

**The dependence of metal-silicate partitioning of moderately volatile elements on oxygen fugacity and Si contents of Fe metal: Implications for their valence states in silicate liquids**

Antje K. Vogel<sup>1,2</sup>, Eleanor S. Jennings<sup>1,3\*</sup>, Vera Laurenz<sup>1</sup>, David C. Rubie<sup>1</sup>, Daniel J. Frost<sup>1</sup>

<sup>1</sup>Bayerisches Geoinstitut, Universität Bayreuth, 95440 Bayreuth, Germany

<sup>2</sup>Lava-Dome, Deutsches Vulkanmuseum Mendig, Brauerstr. 1, 56743 Mendig, Germany

<sup>3</sup>Department of Earth and Planetary Sciences, Birkbeck, University of London, Malet Street, London WC1E 7HX, UK

\*Corresponding author ([e.jennings@bbk.ac.uk](mailto:e.jennings@bbk.ac.uk))

© 2018. This manuscript version is made available under the CC-BY-NC-ND 4.0 license

<http://creativecommons.org/licenses/by-nc-nd/4.0/>

**ABSTRACT**

The volatile siderophile elements are important tracers of the delivery of volatile elements to the Earth. Their concentrations in the bulk silicate Earth are a function of the relative timing of their accretion and their sequestration into the core: a comprehensive understanding of their metal-silicate partitioning behaviour is therefore required in order to infer the volatile element accretion history. We present new partitioning data between liquid metal and liquid silicate at 11 GPa for a suite of volatile siderophile elements: Ag, As, Au, Cu, Ge, P, Pb, Sb, Sn. We focus particularly on determining their valence states and the effects of Si on partitioning, which are required in order to extrapolate from experimental conditions to core-formation conditions. It was found that all elements have weak to strong positive interaction parameters with Si. At low

$fO_2$ , redox equilibria dictate that the siderophile elements should become more siderophile. However, at low  $fO_2$ , Si also partitions more strongly into the metal. Given the repulsive nature of the interaction between Si and the elements of interest, the increased Si concentration at low  $fO_2$  will counteract the expected increase in the partition coefficient, making these elements less siderophile than expected at very reducing conditions. This causes the linear relationship between  $fO_2$  and  $\log(D)$  to become non-linear at low  $fO_2$ , which we account for by fitting an interaction parameter between Si and the elements of interest. This has implications for the interpretation of experimental results, because the valence cannot be determined from the slope of  $\log(D)$  vs.  $\log fO_2$  if low  $fO_2$ , high Si metal compositions are employed without applying an activity correction. This also has implications for the extrapolation of experimental partitioning data to core-formation conditions: reducing conditions in the early stages of core formation do not necessarily result in complete or even strong depletion of siderophile elements when Si is present as a light element in the core-forming metal phase.

Keywords: volatile siderophile elements, valence, partitioning, accretion, core formation

## 1 INTRODUCTION

The Earth is generally considered to have accreted initially from highly reduced material with more oxidized compositions being added later towards the end of accretion (e.g. Wänke, 1981; O'Neill, 1991; Wade and Wood, 2005; Schönbächler et al., 2010; Rubie et al., 2011, 2015). This variation in the composition of accreting material means that the oxygen fugacity under which metal and silicate equilibrated during episodes of core formation varied with time. Thus, in core formation models that are based on multistage or continuous core formation scenarios, oxygen fugacity generally increases with time, in addition to increases in the pressures and temperatures of equilibration between metal and silicate liquids (e.g. Wade and Wood, 2005; Rubie et al., 2011, 2015). Highly reducing conditions are required during the early stages of

accretion in order to satisfy, in particular, the depletion of Earth's mantle in the elements Si, Cr and V relative to chondritic concentrations (Rubie et al., 2011).

During the early, reduced stages of core formation, Si enters the metallic core-forming liquid as is expected according to redox equilibria. In the later stages, the high  $T$  conditions of equilibration mean that Si continues to enter the core-forming metal even when conditions are more oxidising (e.g. Tsuno et al., 2013). As a result, the core is expected to contain a significant concentration of Si, explaining at least some fraction of its density deficit (Allègre et al., 1995; Gessmann et al., 2001; McDonough, 2003; Wood et al., 2006; Ricolleau et al., 2011; Rubie et al., 2011, 2015: estimates cover a wide range of 1-11 wt%, with 7 wt% being consistent with chondritic ratios).

The partitioning of trace siderophile elements into the core is usually investigated experimentally and extrapolated to core-formation conditions. However, it is well known that the presence of certain solutes in liquid iron can affect the stability of others (Wagner, 1952), and that interactions in the metal will change partitioning behaviour (e.g. Wade and Wood, 2005). Tuff et al. (2011) have shown that Si dissolved in the metal can significantly affect the partitioning of some siderophile elements (Ni, Co, Mo, W, V) by making them less siderophile. Similarly, Righter et al. (2017a) identified strong positive (i.e. repulsive) interactions between Si and the volatile siderophile elements As, Sb, Ge and In, which were stronger for some elements than others. Redox equilibria dictate that cations in silicate melts should be more siderophile at more reduced conditions. In light of these findings, one would expect this increased siderophilicity of many elements to be counteracted, at least to some extent, by the Si content of core-forming liquid Fe alloy. As most experiments are performed at lower pressures and/or more oxidising conditions than those of Earth's core-formation, the Si content of the core may not always match that of experiments. The effect of Si on partitioning therefore needs to be described quantitatively using interaction parameters in order to extrapolate experimental results to the conditions of core formation.

The volatile siderophile elements are particularly interesting, as they can constrain the origin and timing of volatile element additions to the Earth: volatile-rich material originating at large heliocentric distances from the Sun could carry water, carbon, sulfur etc. as well as other volatile siderophile elements. The bulk silicate Earth (BSE) is depleted in volatile siderophile elements relative to CI chondrite abundances (Witt-Eickschen et al., 2009). Their concentrations would have been lowered by partitioning into the core (e.g. Wood et al., 2006) and possibly by impact-driven volatilisation (e.g. Witt-Eickschen et al., 2009, Norris and Wood, 2017), but raised by any late additions of volatile-rich material after core formation was complete (e.g. Albarède, 2009). To correctly interpret the BSE volatile element concentrations, and to assess the relative contributions of these two processes, a comprehensive understanding of the metal-silicate partitioning behaviour of these elements is required.

The metal-silicate partitioning systematics of various volatile siderophile elements have been the focus of several recent studies (e.g. Ballhaus et al., 2017; Righter et al., 2017a, b; Steenstra et al., 2017a), with the goal of understanding the systematics of their metal-silicate partitioning behaviour as a function of one or more of pressure, temperature,  $fO_2$  and metal composition. For example, As, Bi, Cd, Ge, In, Sb and Sn were all shown to partition less strongly into metal with increasing temperature by Righter et al. (2017a, b). Metallic S has also been shown to affect partitioning behaviour of Sn and Pb (Ballhaus et al., 2017), and Sb (Steenstra et al., 2017a). The presence of metallic S makes some volatile elements more siderophile, and others less, which is in contrast to the effects of metallic Si identified in previous studies, which appears to always reduce the siderophile tendency of the volatile elements studied. Given that metal-silicate partitioning of volatile siderophile elements involves redox reactions, the  $fO_2$  control is set by the valence state of the cation in the silicate melt.

In order to interpret metal-silicate partitioning results and to apply them to core formation, it is essential to know the valence of each element when dissolved in silicate liquid. The typical method for determining valence is to perform partitioning experiments over a range

of oxygen fugacities at constant  $P$ - $T$  conditions. The valence is then determined from the slope of a plot of  $\log D$  vs oxygen fugacity ( $\log fO_2$ ) where  $D$  is the metal-silicate partition coefficient (e.g. Gessmann et al., 1999). In addition, XANES determinations of valence states have been made for some refractory siderophile elements (e.g. O'Neill et al., 2008), but not of volatile elements. The cationic valence states of some volatile elements remain unknown or poorly constrained. Importantly, Righter et al. (2017a) observed that the silicate cationic valence states of their studied set of volatile elements (Sb, As, Ge and I) at low  $fO_2$  are non-linearly related to the measured partition coefficient, due to effects originating from interaction with metallic Si.

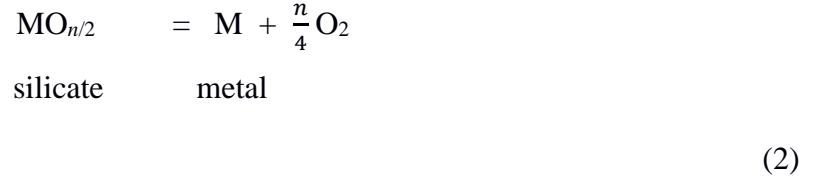
In this study, we have determined the liquid metal – liquid silicate partitioning of the volatile siderophile elements Sn, Pb, Ag, Cu, Ge, P, Sb, As and Au at 11 GPa and 2600 ( $\pm 100$ ) K by performing high pressure experiments in a multianvil apparatus over a wide range of oxygen fugacities ( $\Delta IW$ -2.4 to -5.4). We have quantified valence states and the influence of Si on volatile siderophile element partitioning simultaneously. Interactions between Si and the elements of interest are fitted with interaction coefficients  $\varepsilon_i^k$  that describe the influence of element  $k$  dissolved in Fe metal on the activity of element  $i$  (Ma, 2001). We show that if the effect of Si on the activity coefficients is ignored, derived valences can be seriously in error.

## 2 DEFINITIONS

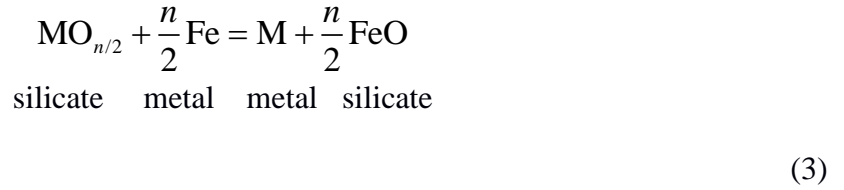
All models of core formation that rely on geochemical constraints are based on experimentally-determined metal-silicate partition coefficients. For element M, the molar metal-silicate partition coefficient is defined as:

$$D_M^{\text{met-sil}} = \frac{X_M^{\text{met}}}{X_{MO_{n/2}}^{\text{sil}}} \quad (1)$$

where the  $X_M^{\text{met}}$  and  $X_{\text{MO}_{n/2}}^{\text{sil}}$  terms are the respective mole fractions of element M and its oxide  $\text{MO}_{n/2}$  in coexisting metal and silicate liquids, respectively. In addition to being dependent on  $P$  and  $T$ ,  $D_M$  is dependent on oxygen fugacity as shown by the equilibrium:



where  $n$  is the valence of element M in the silicate liquid. This equilibrium shows that increasing oxygen fugacity results in decreasing  $D_M$ . By including Fe and FeO:



The equilibrium constant ( $K$ ) of this reaction can be written as:

$$\log K = \log \left[ \frac{X_M^{\text{met}}}{X_{\text{MO}_{n/2}}^{\text{sil}}} \right] + \log \left[ \frac{\gamma_M^{\text{met}}}{\gamma_{\text{MO}_{n/2}}^{\text{sil}}} \right] + \frac{n}{4} \Delta IW \quad (4)$$

where  $X_M^{\text{met}}$  and  $X_{\text{MO}_{n/2}}^{\text{sil}}$  represents the mole fractions of M and  $\text{MO}_{n/2}$  in the metal (met) and silicate (sil) respectively, and  $\gamma_M^{\text{met}}$  and  $\gamma_{\text{MO}_{n/2}}^{\text{sil}}$  represent the activity coefficients of these components. Because oxygen fugacity is related to the Fe redox equilibrium between metal and silicate, the Fe and FeO terms in eq. 4 have been replaced by the oxygen fugacity, referenced to the iron-wüstite buffer:

$$\Delta IW = 2 \log \frac{a_{\text{FeO}}^{\text{sil}}}{a_{\text{Fe}}^{\text{met}}} = 2 \log \frac{(X_{\text{FeO}}^{\text{sil}})(\gamma_{\text{FeO}}^{\text{sil}})}{(X_{\text{Fe}}^{\text{met}})(\gamma_{\text{Fe}}^{\text{met}})} \quad (5)$$

Finally, the exchange coefficient,  $K_D$ , can be formulated as:

$$K_D = \frac{X_M^{\text{met}}(X_{\text{FeO}}^{\text{sil}})^{n/2}}{X_{\text{MO}_{n/2}}^{\text{sil}}(X_{\text{Fe}}^{\text{met}})^{n/2}}$$

(6)

$K_D$  is thus independent of  $fO_2$  but its determination requires knowledge of the valence  $n$ . The equilibrium constant  $K$  of Eq. 4 is related to  $D$ ,  $K_D$  and  $fO_2$  by the inclusion of activity terms. Provided these activity coefficients are constant over the range of compositions studied experimentally, the partition coefficient is related to  $fO_2$  by:

$$\log D_M^{\text{met-sil}} = -\frac{n}{4}\Delta IW + \text{constant} \quad (7)$$

According to Eq. 7, the valence  $n$  can therefore be determined from the slope of  $\log(D_M^{\text{met-sil}})$  plotted against  $\Delta IW$ .

### 3 METHODS

#### 3.1 Experiments

Partitioning experiments were performed at 11 GPa and 2600 ( $\pm 100$ ) K in a multianvil apparatus. Starting materials consisted of different combinations of metal and peridotite-composition powders. The metal phase consisted of either Fe, Fe + FeO, Fe<sub>91</sub>Si<sub>9</sub>, or Fe<sub>83</sub>Si<sub>17</sub> (wt. proportions) to which the elements of interest were added either as pure elements or oxides in quantities between 0.5 and 3 wt% (Table S1, supplementary information). The trace elements were added in groups (1: Cu, Ge, Sb, Sn; 2: As, Au, P; 3: Pb; 4: Ag) such that no more than four trace metals were investigated in any given run. The components of the metal phases were mixed, ground under ethanol and subsequently dried.

The peridotite silicate starting material consisted of 48.3 wt. % SiO<sub>2</sub>, 39.1 wt.% MgO, 4.8 wt.% Al<sub>2</sub>O<sub>3</sub>, 3.9 wt.% CaO and 3.8 wt. % FeO, and was based on the primitive mantle composition of Palme and O'Neill (2003). The FeO content is approximately half the published value: this was chosen to balance the FeO increase caused by reaction with Fe metal during the experiments. Prior to its preparation, all oxides were heated at 1000 °C for one hour in order to

remove any adsorbed water, except for  $\text{CaCO}_3$  and  $\text{Al}_2\text{O}_3$ , which were heated at 120 °C for three hours. After cooling, the powders were weighed, mixed, ground under ethanol and subsequently dried. FeO and CaO were added as  $\text{Fe}_2\text{O}_3$  and  $\text{CaCO}_3$  respectively. Subsequent reduction and decarbonation at an oxygen fugacity 2 logarithmic units below the FMQ buffer in a CO–CO<sub>2</sub> atmosphere at 1000 °C or 1100 °C in a 1 atm gas-mixing furnace ensured that the desired composition was achieved and that all iron was present as  $\text{Fe}^{2+}$ . This is important because siderophile elements, and especially the highly siderophile elements like Au, are known to form nano-nuggets in the silicate melts (e.g. Ertel et al. 2008, Laurenz et al. 2013) that pose a problem for later LA-ICP-MS analysis of the run products (e.g. Ertel et al., 2008; Laurenz et al., 2013). Such nuggets exsolve if  $f\text{O}_2$  is higher at the start of an experiment compared to equilibrium conditions (e.g. Ertel et al. 2008; Bennett et al. 2014; Médard et al. 2015) because metal solubility in silicate melts decreases with decreasing  $f\text{O}_2$ . Using a reduced silicate starting composition successfully minimizes the formation of such nano-nuggets in the silicate liquid (Médard et al., 2015), because the  $f\text{O}_2$  is already low at the beginning.

All experiments were performed in a multianvil apparatus, either a 5000 tonne Zwick press or a 1000 tonne Hymag press (indicated by either a “Z” or “H” preceding the identification numbers of the experiments; calibrations of Frost et al., 2004 and Rubie et al., 1993, were used respectively). The sample assembly consisted of an 18 mm edge-length  $\text{Cr}_2\text{O}_3$ -doped MgO octahedron that was compressed by eight WC cubes with 11 mm truncations. A stepped  $\text{LaCrO}_3$  heater was used to minimize temperature gradients (Rubie, 1999) and temperature was measured using a type D  $\text{W}_{97}\text{Re}_3$ – $\text{W}_{75}\text{Re}_{25}$  thermocouple. The metal and silicate powders were loaded into an MgO capsule such that a layer of metal was sandwiched between two layers of silicate powder (Fig. 1c): this configuration was found to facilitate the formation of a single large metal sphere when the sample melted. Each experiment contained two polycrystalline MgO sample capsules (containing different compositions) that were separated by a single crystal MgO disk (Fig. 1a). Pressures were increased slowly to the desired value over a period

of 200 to 280 minutes. Maximum pressures were maintained for 1 hour and the subsequent decompression lasted for 850 to 1000 minutes. The samples were heated at a rate of around 100–200 K per minute, with a higher rate above 1773 K. In most cases the samples were held for 10 minutes at 1773 K in order to allow the sample assembly to stabilize at high temperature. The peak temperature of 2580–2668 K was maintained for a period of 1 to 3 minutes. The run time chosen was guided by previous studies at similar  $P$ – $T$  conditions that have shown durations of 120 s to be sufficient to reach equilibrium (e.g. Thibault and Walter, 1995; Corgne et al. 2008; Mann et al., 2009). Temperature was calculated for each experiment from the output power by using a power-temperature curve that had been fitted to the hottest stable and successful run (measured by thermocouple) in each of the respective multianvil presses. A temperature uncertainty of  $\pm 100$  K has been assumed for all experiments based on known thermal gradients (Rubie, 1999) and the reproducibility of many power-temperature curves from the same laboratory. The experiments were rapidly quenched by switching off the electrical power, initially cooling at a rate of  $\sim 250$  K/s.

### **3.2 Analytical Techniques**

The recovered experimental capsules were mounted in epoxy, ground with SiC paper and polished with diamond grit down to 0.25  $\mu\text{m}$ . In a successful experiment, a sphere of liquid metal develops that is surrounded by quenched silicate liquid. After quenching, the latter exhibits elongated skeletal olivine quench crystals (Fig. 1a). Reaction between the MgO capsule and silicate liquid leads to the formation of ferropericlasite crystals at the capsule wall and occasionally around the quenched metal sphere (Fig. 1a). Quenched metal was analysed quantitatively using a JEOL JXA-8200 electron probe micro-analyser (EPMA). The concentrations of all elements in the silicate were measured using a laser ablation inductively coupled plasma mass spectrometry (LA-ICP-MS) system consisting of an Elan DRC-e

quadrupole mass spectrometer (Perkin Elmer Instruments, Canada) connected to a GeolasPro 193 nm ArF Excimer Laser System (Coherent Inc., USA).

### *3.2.1 Electron Probe Micro-analyser*

For the EPMA measurements the accelerating voltage and the beam current were set to 15 kV and 15 nA respectively. The peak counting times were fixed at 20 s for every element on the peak position and 10 s for all background measurements. The metal phases were analysed in wavelength-dispersive mode with a defocused electron beam usually with a diameter of 20  $\mu\text{m}$ . In some cases, for smaller metal spheres, diameters of 5 or 10  $\mu\text{m}$  were used. Pure metals were used as standards for Fe, Cu, Ge, Ag, and Au, whereas MgO, SnO<sub>2</sub>, PbTe, InAs and apatite were used for O, Sn, Pb, As and P, respectively. Matrix corrections were performed using the  $\phi(\rho z)$ -routine. The number of measurements of the metal phase of each sample ranged from 26 to 63 analyses, depending on the size of the metal spheres (Table S2 supplementary information). Occasionally, quenching of the samples led to the exsolution of a second metallic phase rich in heavy elements such as Ag, Au and Pb, identifiable in a backscattered electron (BSE) image by small bright round blobs contained in the metal matrix (Fig. 1b). Moreover, O and Si were also found to exsolve in some cases from the metal phase, forming round blobs that appear dark in BSE images. Both kinds of exsolution were relatively small and uniformly distributed. Therefore, the use of a broad defocused electron beam together with the combination of a large number of multiple analyses was found to facilitate the determination of the bulk composition of the metal phase. An exsolution-free border region occasionally formed in the metal sphere adjacent to the silicate liquid (similar to that described by O'Neill et al., 1998 and Gessmann and Rubie, 1998). This was interpreted to have formed due to re-equilibration between the metal and silicate liquids during quenching. When compositionally different from the rest of the bulk metal phase, this border region was avoided when analysing the metal.

### 3.2.2 Laser Ablation Inductively Coupled Plasma Mass Spectrometry

When performing LA-ICP-MS analyses of the silicate phases, the sample chamber was flushed with helium gas at a rate of 0.4 l/min that was complemented by Ar gas and H<sub>2</sub> gas with rates of 0.95 l/min and 5 ml/min respectively. The background was measured once before measuring each set of standards and each set of sample measurements with the measuring times on background and signal lasting between 10 s and 40 s. A beam diameter of 80 μm at a frequency range between 5 – 7 Hz was used in order to take account of the often coarse-grained heterogeneous quench structures of the silicate melt (Table S2, supplementary information). Isotopes recorded were <sup>23</sup>Na, <sup>25</sup>Mg, <sup>27</sup>Al, <sup>29</sup>Si, <sup>31</sup>P, <sup>39</sup>K, <sup>42</sup>Ca, <sup>53</sup>Cr, <sup>57</sup>Fe, <sup>65</sup>Cu, <sup>72</sup>Ge, <sup>75</sup>As, <sup>90</sup>Zr, <sup>98</sup>Mo, <sup>107</sup>Ag, <sup>118</sup>Sn, <sup>121</sup>Sb, <sup>139</sup>La, <sup>184</sup>W, <sup>185</sup>Re, <sup>197</sup>Au, <sup>208</sup>Pb. Chromium, La, W and Re were monitored in order to exclude possible contamination of the samples by the W-Re thermocouple and the LaCrO<sub>3</sub> heater. The integrated signal intensities were referenced to the external standard NIST SRM 610 (Jochum et al., 2011) that was measured before and after all other measurements. The derived element ratios were converted into absolute abundances by normalizing the oxides SiO<sub>2</sub>, CaO, FeO, Al<sub>2</sub>O<sub>3</sub> and MgO to total 100 wt.%; concentrations of all other trace elements are reported as ppm abundances (Supplementary Table S2). Sometimes nano-nuggets were visible in the laser spectra as spikes in the signal. These are thought to represent equilibrium phases at run conditions (e.g. Bennett et al., 2014; Médard et al. 2015), and were thus excluded for quantification of trace element concentrations (Ertel et al., 2008).

The USGS silicate glass standards BCR-2G and NKT-1G were periodically measured, with counts converted to abundances using published Al<sub>2</sub>O<sub>3</sub> concentrations as internal standards (Supplementary Table S3; Jochum et al., 2005, 2011; Hu et al., 2011). Most absolute concentrations showed < 10 % differences with published quantities in BCR-2G (except K, Cu, Sn and W, that were < 20 %, and Ge, Ag and As, that were > 20 %).

Reproducibility between measurements in different analytical sessions was excellent, with the relative standard deviation of most elements being  $< 5\%$ .

## 4 RESULTS

A summary of experimental conditions and results is listed in Table 1, which also provides  $D^{met-sil}$  partition coefficients, as well as experimental  $fO_2$  ( $\Delta IW$ ) values, that were determined by the metal-silicate partitioning of Fe (Eq. 5). A complete list of the compositions of the various phases in the experimental samples is provided in Table S2 (supplementary information). The experimental results are plotted as a function of  $X_{Si}$  and  $fO_2$  ( $\Delta IW$ ) in Fig. 2. A detailed account of the data processing and fitting, oxygen fugacity calculation, and valence state preferences on an element-by-element basis, are given in the following sections, along with a discussion of the results.

Literature data were not used in the data fitting (differences in experimental  $P$ ,  $T$  and compositions may cause offsets with our data), but are also shown in Fig. 2 for context and comparison. Previously published  $D_M$  and  $fO_2$  values are recalculated by us for consistency using equations 1 and 5. We only show data points for carbon-free experiments, as carbon interaction in carbon-saturated metal arising from equilibration with graphite capsules can drastically alter  $D_M$  for some elements (e.g. Jana and Walker, 1997a; Chabot et al., 2006; Siebert et al., 2011). Sulfur can also significantly affect trace element activities (e.g. Jana and Walker, 1997b; Wood et al., 2014; Laurenz et al., 2016), so only experiments with low sulfur contents in the metal are shown. A detailed discussion for each element is given in section 4.4 below.

### 4.1 Variations of $D$ with $fO_2$ : the role of Si and valence

The liquid metal – liquid silicate partitioning of an element  $M$  with a valence  $n$  when dissolved in the silicate melt is described by an exchange reaction that involves Fe (Eq. 3), meaning that  $fO_2$  (related to  $D_{Fe}$ ) and  $D_M$  are intrinsically linked. If we begin by assuming ideal mixing and

neglect the activity terms, then Eq. 6 shows that  $\log(D_M)$  should plot as a straight line against  $\log fO_2$  with a slope equal to  $(-n/4)$ . Fig. 2a-i shows  $D_M$  for all elements as a function of  $\log fO_2$ . Rather than defining a linear trend, many elements fall on a curve.  $D_M$  should be greatest at lowest  $fO_2$ , but appears suppressed to lower values for many elements.

Low  $fO_2$  conditions result in high concentrations of Si entering the metal or, stated alternatively, the existence of high metallic Si contents decreases the experimental  $fO_2$ . In this study and others,  $Fe_{(1-x)}Si_x$  alloys were used in the experimental starting compositions specifically to access low  $fO_2$  conditions. Because  $X_{Si}$  and  $fO_2$  are correlated (Fig. 3), the change in activity coefficient of a trace element caused by changing the silicon content will be convoluted with the effect of valence on partitioning. Fig. 2a-i also shows  $K_D$  (the exchange coefficient) as a function of  $X_{Si}$  in the metal. For a given assumed fixed valence state, this value should be constant with varying  $fO_2$ , because  $fO_2$  is explicitly accounted for in its formulation (Eq. 4). As expected from the non-linear relationship between  $\log(D_M)$  and  $fO_2$ ,  $K_D$  decreases with increasing  $X_{Si}$  (decreasing  $fO_2$ ) to some extent for every element. There are three possible explanations: 1) the valence state has changed (decreased) at low  $fO_2$ ; 2) the assumption that variations in activity terms are negligible is invalid; 3) changes in the silicate composition are responsible.

We reject the idea that a drop in valence state is responsible for suppressing  $D$  at low  $fO_2$  because it is highly unlikely that every element experiences a change in valence at a similar  $fO_2$ , and also many of the elements studied are not known to be heterovalent over the experimental  $fO_2$  range (as reviewed in section 4.4). We can also dismiss the idea that changes in the silicate melt composition are responsible. The same starting silicate was used in all experiments, and there is no systematic difference between the silicate melt compositions of different run products except in their FeO content (the other oxides are all a little more concentrated in low FeO silicates, with no changes in relative proportions), which is a necessary

consequence of changing  $fO_2$  and is already explicitly accounted for in the formulation of  $K_D$  and  $K$ .

The alternative and simplest explanation is that changes in the trace element activity coefficients in the metal are responsible. Mixing in liquid metallic alloys is known to be strongly non-ideal. Previous studies have shown that interactions with Si in the metal can strongly affect the propensity for other solutes to enter the metal (Chabot et al., 2010; Tuff et al., 2011; Righter et al., 2017a). Righter et al. (2017a) specifically show that Si in the metal decreases the siderophility of three volatile siderophile elements examined in this study: Ge, As and Sb. Our lowest  $fO_2$  experiments also contain the highest  $X_{Si}$  metals (Fig. 3): thus, Si has a positive interaction with the trace element of interest such that one ejects the other, causing a decreasing siderophility of the trace element.

The magnitude of the effects of  $X_{Si}$  on  $D_M$  are quantified by fitting an interaction parameter,  $\epsilon_M^{Si}$ , to the data, as described in the following section. Because the valence states of the volatile siderophile elements are not independently constrained, the competing effects of valence and silicon interaction on  $D_M$  must be jointly considered. Previous studies performed at  $fO_2$  conditions greater than those where silicon begins to enter the metal (approx.  $\Delta IW-2.5$  at 11 GPa) can provide valuable additional constraints on the valence state, as in these cases the slope of  $\log(D_M)$  plotted against  $\log fO_2$  should reflect the true valence state, as long as the pressure, temperature, and metal or silicate compositions are not changing significantly within a series of experiments. In addition, we know from stable electron configurations that not every possible valence state is equally likely to be stable for cations in the silicate melt.

## 4.2 Determination of interaction parameters $\epsilon_M^{Si}$ and valence states

At chemical equilibrium, the Gibbs free energy change  $\Delta G^\circ$  is related to the equilibrium constant  $K$  by:

$$\Delta G^\circ = -RT \ln K$$

(8)

Assuming that the ratio of activity coefficients of oxide components in the silicate liquid are constant over the narrow range of silicate melt compositions in our experiments, the equilibrium constant  $K$  (Eq. 6) of the exchange reaction (Eq. 3) is a function of Fe and trace element mole fractions in the metal and silicate phases, and activity terms in the metal only. Accepting this assumption and rearranging equations 1, 5 and 8 leads to:

$$\log D_M^{\text{met-sil}} = \frac{-\Delta G^\circ}{RT \ln(10)} - \log(\gamma_M^{\text{met}}) - \frac{n}{2} \log(X_{\text{FeO}}^{\text{sil}}) + \frac{n}{2} \log(X_{\text{Fe}}^{\text{met}} \gamma_{\text{Fe}}^{\text{met}}) \quad (9)$$

This allows for the valence state  $n$  of an element M, as well as the activity coefficients, to be determined given a sufficient range of  $\log(D^{\text{met-sil}})$  and  $X_{\text{FeO}}$  measurements and an activity-composition model for M and Fe in the metal. The value of  $\gamma_M^{\text{met}}$  varies over the compositional range mainly as a function of the metal Si content.

We calculate the activity coefficients of Fe ( $\gamma_{\text{Fe}}^{\text{met}}$ ) and the element of interest M ( $\gamma_M^{\text{met}}$ ) in the metal by considering non-ideal interactions, using the  $\epsilon$ -model as formulated by Ma (2001), following Wade and Wood (2005). The method is described in the Appendix. This approach uses interaction parameters  $\epsilon_i^k$  (Wagner, 1952) to describe the influence of the concentrations of one or more elements ( $j, k, \dots$ ) on the activity of a given solute element  $i$ . We have applied this approach to a ternary alloy consisting of Fe, Si and the element of interest M. The activity coefficients  $\gamma_M$  and  $\gamma_{\text{Fe}}$  are calculated using equations A1 and A2. To calculate  $\gamma_M^{\text{met}}$  and  $\gamma_{\text{Fe}}^{\text{met}}$ , the interaction parameters  $\epsilon_{\text{Si}}^{\text{Si}}$ ,  $\epsilon_M^{\text{M}}$ , and  $\epsilon_M^{\text{Si}}$  are required, as well as the activity coefficient of element M at infinite dilution ( $\gamma_M^0$ ):  $\epsilon_{\text{Si}}^{\text{Si}}$  is taken from the Steelmaking Data Sourcebook (J.S.P.S., 1988);  $\epsilon_M^{\text{M}}$  and  $\ln(\gamma_M^0)$  are taken from J.S.P.S. (1988) when known, or are otherwise set to 0 (ideal mixing);  $\epsilon_{\text{Si}}^{\text{Si}} = 8.6$ , from Tuff et al. (2011);  $\epsilon_M^{\text{Si}}$  is fitted as an unknown. The terms  $\epsilon_{\text{Si}}^{\text{Si}}$ ,  $\epsilon_M^{\text{M}}$ ,  $\gamma_M^0$  and  $\epsilon_M^{\text{Si}}$  are constant at a given pressure and temperature, and their temperature dependencies are defined by Eq. A3 and A4.

Our aim is to determine the valence state and silicon interaction term  $\varepsilon_M^{\text{Si}}$ , which exerts the main control over  $\gamma_M^{\text{met}}$ , of each trace element studied. All experiments were performed at isobaric (11 GPa) and near-isothermal ( $2600 \pm 100$  K) conditions with near-identical silicate compositions, so  $\Delta G^\circ$  for a given reaction should be constant for all experiments: if they are not, the activity terms cannot be correct. We can exploit this fact to fit the only unknown variable in the activity corrections,  $\varepsilon_M^{\text{Si}}$ , with a value that forces the calculated  $\Delta G^\circ$  of all experiments to equal that of a Si-free reference experiment. Our approach for each element is as follows:

- 1) We first determine  $\Delta G^\circ$  for a reference experiment of each trace element with a nominally Si-free metal (i.e. a nominally binary alloy, where there is zero effect from Si interaction — usually the most oxidised experiment). This was done by solving Eq. 8 for the experiment with the lowest  $X_{\text{Si}}$  ( $X_{\text{Si}}$  usually  $< 0.002$ ) for a chosen valence. All activity terms needed for this calculation are known.
- 2) For the remaining experiments, we began with an initial guess for  $\varepsilon_M^{\text{Si}}$ , and used this to calculate  $\gamma_{\text{Fe}}^{\text{met}}$  and  $\gamma_M^{\text{met}}$ . With these activity coefficients, we calculated a predicted  $D_M$  using Eq. 9, and defined the difference (mismatch) between the predicted and actual measured  $D_M$  as the root mean square (RMS) uncertainty. We then found an optimum value for  $\varepsilon_M^{\text{Si}}$  that minimised the RMS: this is referred to as our fitted value. The remaining RMS uncertainty after fitting each trace element is shown in Fig. 4.
- 3) Steps 1 and 2 are repeated for a range of different assumed valence states  $n$ : we consider that the valence state resulting in the lowest residual error after fitting  $\varepsilon_M^{\text{Si}}$  is most likely to be correct. The remaining residual error at the most likely valence state is likely due to small but unquantified changes in activity coefficients in the silicate melt resulting from changes in the silicate FeO content, as well as experimental and analytical uncertainties.

If unknown and thus set to zero, the values of  $\varepsilon_M^M$  and  $\ln(\gamma_M^0)$  become part of the calculated  $\Delta G^\circ$ , which we continue to refer to as  $\Delta G^\circ$  for simplicity. Table 2 summarises the values used from J.S.P.S (1988) and the fitted results:  $\Delta G^\circ$ , RMS uncertainties and  $\varepsilon_M^{\text{Si}}$  (referenced to 1873 K) for our preferred valence state. Uncertainties on  $\varepsilon_M^{\text{Si}}$  were found by determining the difference in  $\varepsilon_M^{\text{Si}}$  required to raise or lower the mean  $\log(D)$  by  $1\sigma$  (approximated by RMS) for a given valence. The best fit  $\varepsilon_M^{\text{Si}}$  varies linearly with  $n$ . We therefore also provide equations in Table 2 expressing  $\varepsilon_M^{\text{Si}}$  as a linear function of  $n$ , should an interested reader want to use our interaction parameters but disagree with our assessment of the valence state.

### 4.3 Calculation of oxygen fugacity

The oxygen fugacity of a given experiment relative to the iron-wüstite buffer ( $\Delta IW$ ) is calculated from Fe redox equilibrium between silicate melt and metal according to Eq. 5, assuming that the activity of FeO in the silicate is equal to its mole fraction, and calculating the activity of Fe in the metallic liquid using the epsilon model (Ma, 2001; see appendix 1) and our newly-determined  $\varepsilon_M^{\text{Si}}$  values (note that calculated  $fO_2$  is not used in fitting the  $\varepsilon_M^{\text{Si}}$  terms). Although the activity coefficient of FeO in a silicate liquid ( $\gamma_{\text{FeO}}^{\text{sil}}$ ) is unlikely to be 1, this approximation has been widely used in previous studies (e.g. Asahara et al., 2004; Ballhaus et al., 2013; Fischer et al., 2015). We chose this approach rather than constraining FeO activity from the composition of ferropericlase, because although ferropericlase is present in all experiments, the composition of this phase in a given sample is highly variable (the typical relative standard deviation of FeO concentrations is around 30 %). Quenched diffusion rims and disequilibrium capsule grains may be responsible and make the identification of the equilibrium composition of ferropericlase difficult to determine. In addition, calculating  $fO_2$  using the silicate melt composition allows direct comparison with literature data. The calculated  $fO_2$  ranges from  $\Delta IW$ -5.4 to -2.4 (Table 1). If  $\gamma_{\text{FeO}}^{\text{sil}}$  is instead taken to be 1.7, as found by

Holzheid et al. (1997), calculated  $\Delta IW$  values would systematically increase by around 0.5, which would not affect our conclusions.

#### 4.4 Results for individual elements

##### 4.4.1 Copper

$\log(D_{\text{Cu}})$  at a given  $f\text{O}_2$  from our study is consistent with results of previous experimental studies performed using MgO capsules (Fig. 2; Wood et al., 2008; Righter et al., 2010). This is despite the published experiments being performed at lower pressures (1 and 2 GPa respectively) and temperatures (both under 2200 K) than those of this study. Righter et al. (2010) showed that  $D_{\text{Cu}}$  is not particularly sensitive to temperature, and the present comparison also suggests a lack of sensitivity to pressure and silicate melt composition.

Our best fit (lowest RMS) for copper is found when a low valence state is assumed, with a minimum at  $n = 1$  (Fig. 4). A low valence of 1+ ( $\text{Cu}_2\text{O}$ ) in silicate melts is in agreement with the findings from Fe-free solubility studies at  $f\text{O}_2$  relevant to core-formation conditions (Holzheid and Lodders, 2001) and regression of  $\log(D_{\text{Cu}})$  as a function of  $f\text{O}_2$  by Righter and Drake (2000) and Corgne et al. (2008). Wood et al. (2008) also assumed a 1+ valence state without explicitly testing for it. Taking  $n = 1$ , a correspondingly low  $\epsilon_{\text{Cu}}^{\text{Si}}$  of  $1.5(\pm 1.1)$  is required to best fit the experimental data to the model  $\Delta G^\circ$  calculated from a nominally metallic-Si-free experiment (Table 2). This means that minimal interaction with Si is required to explain the Cu partitioning behaviour, and is a little lower than the value for  $\epsilon_{\text{Cu}}^{\text{Si}}$  of 3.6 given by the Steelmaking Data Sourcebook (J.S.P.S., 1988).

##### 4.4.2 Silver

Silver is moderately siderophile, with values of  $\log(D_{\text{Ag}})$  of around 1.5; there are no published data in C-free systems for comparison with our results. The best fit (lowest RMS) valence state is 1+, although it is barely distinguishable from 0 (Fig. 4). This is in agreement with the valence

determined by 1-atm solubility experiments by Capobianco et al. (1994), who interpreted  $\text{Ag}^+$  to be stable in silicate melts but could not rule out a zero-valence contribution at  $f\text{O}_2$  relevant to core-formation conditions. A small  $\varepsilon_{\text{Ag}}^{\text{Si}}$  value of  $5.0(\pm 1.3)$  is determined for our preferred valence state of 1+ (Table 2).

#### 4.4.3 Lead

A valence of 2+ (PbO) best fits our partitioning data, with a corresponding  $\varepsilon_{\text{Pb}}^{\text{Si}} = 10.2(\pm 0.9)$ . This is consistent with previous partitioning studies, which also identified (Malavergne et al., 2007; Wood and Halliday, 2010), or assumed (Lagos et al., 2008; Wood et al., 2008), a 2+ oxidation state. In contrast, Bouhifd et al. (2013) found a 1+ valence through a multiple linear regression of a data compilation. However, our study suggests that the lower valence of Bouhifd et al. (2013) may result from their inclusion of some very low  $f\text{O}_2$ , high  $X_{\text{Si}}$  experiments in their regression, which will depress  $D$  and thus affect the valence determination. Fig. 2 shows literature data along with our new data (only literature data from C-free and low S experiments are shown, as C and S in metal will reduce the siderophility of Pb; Wood and Halliday, 2010; Ballhaus et al., 2017). Our results are not expected to show good agreement with the literature data because of the strong dependence of  $D_{\text{Pb}}$  on temperature (Ballhaus et al., 2013). Despite this, our new data are in good agreement with published low-sulfur partition coefficients (Wood et al., 2008; Ballhaus et al., 2013, 2017; Steenstra et al., 2017a), except for the single high  $X_{\text{Si}}$  data point of Bouhifd et al. (2013).

#### 4.4.4 Gold

The 1-atm solubility experiments of Borisov and Palme (1996) indicate that Au is present as  $\text{Au}_2\text{O}$  in silicate melts when the  $f\text{O}_2$  is higher than approximately IW. However, at more reducing conditions, a dramatic change in solubility was interpreted by the authors to indicate

that Au has a negative charge, for example being incorporated as  $\text{AuSi}_x$ , in the melt. Brenan and McDonough (2009) later agreed with this assessment, as  $\log(D_{\text{Au}})$  from their metal-silicate partitioning experiments decreased slightly with decreasing  $f\text{O}_2$ , requiring  $\text{Au}^0$  or  $\text{AuSi}_x$  stability. The partitioning experiments were performed at more oxidising conditions than those of the present study, so Si in the metal cannot be responsible for lowering  $D_{\text{Au}}$ . Danielson et al. (2005) fitted a small positive formal valence (+0.5) to Au partitioning data by multiple regression of partitioning experiments over an  $f\text{O}_2$  range of  $\Delta\text{IW}$  -1.2 to -2.5. We find that  $D_{\text{Au}}$  has the lowest residual error when fitted with  $n = 1+$  (Fig. 4). Although the literature data are in disagreement with one another, they all indicate a low valence for gold. Our preferred valence for gold in silicate melts during core formation is  $1+$ , and on this basis,  $\epsilon_{\text{Au}}^{\text{Si}} = 12.0(\pm 5.2)$ . We cannot rule out that the change in slope of  $D_{\text{Au}}$  at low  $f\text{O}_2$  is due to a reduction of gold rather than an activity effect from metallic silicon. However, it seems unlikely that neutral Au atoms would bond in the silicate melt structure (although Bennett et al. (2014) suggest that  $\text{Pt}^0$  is stable in silicate solubility experiments), and we would expect partitioning with  $\text{Au}^0$  to have no  $f\text{O}_2$  dependence rather than the observed positive slope. Literature data only exist for graphite capsule experiments and so cannot be directly compared with our data, because the high concentrations of carbon in the metal will substantially alter the siderophilicity of gold (and many other siderophile elements) (Chabot et al., 2006).

#### 4.4.5 Tin

Our new data can be fitted equally well by assuming a  $2+$  or  $3+$  valence, which correspond to  $\epsilon_{\text{Sn}}^{\text{Si}} = 12.2(\pm 4.9)$  and  $19.9$ , respectively (Fig. 4; Table 2), i.e. Si causes a large decrease in the siderophilicity of Sn. Our low  $X_{\text{Si}}$ , high  $f\text{O}_2$  data are in moderate agreement with published low-S and nominally metallic Si-free partitioning data (all at 1–2 GPa and 1773–2273 K: Righter et al., 2010; 2017b; Ballhaus et al., 2013, 2017) in terms of  $\log(D)$  as function of  $f\text{O}_2$ , although the single data point shown from Righter et al. (2009) lies far from our trend (Fig. 2e).

Capobianco et al. (1999) performed 1 atm partitioning experiments between solid metal and liquid silicate, and found Sn to be tetravalent at higher  $fO_2$ , ( $> \Delta IW \sim -2$ ), switching to predominantly divalent Sn at lower  $fO_2$  ( $< \Delta IW \sim -2$ ). They also noted that the apparent valence state determined from partitioning data can be misleading: in their study, changes in trace metal activity resulted from the changing metal composition (in their case, changing Fe:Ni), and the true valence state only became apparent after activity corrections had been made, which is consistent with our findings. Righter and Drake (2000) performed a regression of activity-corrected  $\log(D_{Sn})$  and determine the silicate valence to be  $Sn^{4+}$ . This high valence may be expected given the results of Capobianco et al. (1999) and the fact that the experiments of Righter and Drake (2000) span  $fO_2 = \Delta IW -2.5$  to  $+0.8$  and the regression returns a single valence state. Our preferred valence state for Sn is  $2+$  at  $\Delta IW < -2$ .

#### 4.4.6 Germanium

Our data are best fit by a valence of  $3+$  for Ge, although the difference in RMS between all valence states is small, meaning that the present data do not rule out other valence states ( $2+$  to  $4+$ ; Fig. 4). At the more oxidised conditions relevant for magmatism at the Earth's surface, Ge is tetravalent in silicate materials and substitutes directly for Si (Bernstein, 1985). At more reduced 1 atm. conditions (although still oxidising relative to core formation conditions;  $\Delta IW -1.3$  to  $+3.5$ ), Capobianco et al. (1999) also found a valence of  $4+$  after applying large activity corrections to their data. At reduced conditions that are more relevant to core formation ( $\Delta IW +0$  to  $-2.5$ ), Schmitt et al. (1989) determine a valence of  $2+$  from 1-atm partitioning experiments in the gas-mixing furnace, where  $fO_2$  was determined precisely using a  $ZrO_2$  sensor. High pressure partitioning experiments indicate that Ge is in the reduced form of either  $Ge^{2+}$  (Kegler and Holzheid, 2011; Righter et al., 2011, 2017a) or  $Ge^{3+}$  (Siebert et al., 2011) from regression of  $\log(D_{Ge})$  as a function of  $fO_2 \pm$  other variables: as these experiments are all more oxidised than  $\Delta IW -3.3$  (most experiments were more oxidizing than  $\Delta IW -2.5$ ), we can assume that these

slopes are not significantly affected by the presence of metallic Si. In summary,  $\text{Ge}^{2+}$  is expected from the literature at core-formation conditions, and this value is consistent with our findings. Our preferred silicate species at core-formation conditions is therefore GeO, which requires moderate interaction with metallic Si ( $\epsilon_{\text{Ge}}^{\text{Si}} = 12.2(\pm 6.3)$ ) to explain the deviation of  $\log(D_{\text{Ge}})$  and  $\log(K_{\text{D}})$  at low  $f\text{O}_2$  (Fig. 2). The slopes of the literature data are in good agreement with ours, although there is a small offset in absolute  $\log(D)$  (Fig. 2), perhaps due to the pressure and/or temperature differences between the datasets. The experiments of Kegler and Holzheid (2011) were performed at a temperature almost 1000 K cooler than ours, which, according to the moderately strong temperature dependence of Siebert et al. (2011), should result in their  $\log(D_{\text{Ge}})$  values being offset from ours by around +0.8.

#### 4.4.7 Antimony

$\log(D_{\text{Sb}})$  from this study has two solutions: equally good fits exist for 3+ and 4+ (Fig. 4), corresponding to fairly large interactions with Si described by  $\epsilon_{\text{Sb}}^{\text{Si}} = 22.6(\pm 10.6)$  and  $30.2(\pm 14.1)$ , respectively. Righter et al. (2009) performed solid and liquid metal – liquid silicate partitioning experiments on Sb, and after applying activity corrections for Ni in the metal, determine the dominant silicate species to be  $\text{Sb}_2\text{O}_3$  over an  $f\text{O}_2$  range of around  $\Delta\text{IW} = -1.5$  to  $+2.5$ . Righter et al. (2017a) also found a 3+ oxidation state for Sb by fitting additional high pressure, lower  $f\text{O}_2$  partitioning data. However, because they first fitted  $\epsilon_{\text{Sb}}^{\text{Si}}$  by assuming  $\text{Sb}^{3+}$ , then used this to calculate an activity correction before fitting the valence, the valence was not independently determined. Our preferred valence for antimony in silicate melts during core-formation is 3+. Our data are compared with the S-poor, MgO-capsule data of Righter et al. (2009, 2017a, 2017b) and Steenstra et al. (2017a) in Fig. 2; the reasons for discrepancies with the data of Righter et al. (2009, 2017a) are unclear, although the uncertainty in the determination of  $f\text{O}_2$  from metal Fe – silicate FeO equilibria at very low  $f\text{O}_2$  (the literature data reach  $\Delta\text{IW} = -8$ )

is large. Experimental pressure and temperature differences are not obviously responsible, as Righter et al. (2009) and Steenstra et al. (2017a) use similarly low  $PT$  conditions as one another ( $< 2000$  K and  $< 2.5$  GPa) yet their reported  $\text{Log}(D_{\text{Sb}})$  values vary substantially.

#### 4.4.8 Phosphorus

Phosphorus is almost always considered to have a high valence of 5+ in the literature, and usually occurs in this state in melts and minerals at low-pressure conditions. Siebert et al. (2011) determine a 5+ valence from their high pressure partitioning experiments, and because their experiments contain negligible Si or S in the metal,  $\log(D_{\text{P}})$  is not expected to deviate much from the trend defined by valence. This therefore seems a good estimate of the true valence of P in high pressure silicate melts at conditions more reducing than IW. Newsom and Drake (1983) also found steep slopes of  $\log(D_{\text{P}})$  as a function of  $f\text{O}_2$ , at 1 atm and over a similar  $f\text{O}_2$  range to Siebert et al. (2011) ( $\Delta\text{IW} = -1$  to  $-2$ ), implying a valence of +5 to +6. However, Righter et al. (2010) found a mean valence of +2.7 from multiple linear regression analysis of 1 GPa experiments, and Righter and Drake (2000) fitted a valence of +4.2 in a similar manner, both also over a similar  $f\text{O}_2$  range of approximately  $\Delta\text{IW} = -1$  to  $-2$ . Determining valence by multiple linear regression risks convoluting the valence effect on  $\log(D_{\text{P}})$  with that of correlated parameters, and such a low valence is inconsistent with known P geochemistry, so we consider the high valence estimates of the other studies to be more reliable. The determination of valence of any element by multiple linear regression should be approached with caution, particularly for high valence elements such as W.

In the present study, the best fit (lowest mismatch) valence for P is 2+ (Fig. 4). However, we do not consider this value to be reliable or realistic. As discussed below, in Fig. 5 the four data points for P partitioning all fall on different valence prediction curves, meaning that the four experiments do not represent a coherent result. The literature data and electronic configuration arguments clearly point to  $\text{P}^{5+}$  in silicate melts, and we accept a value of 5+ rather

than the lowest uncertainty result. If  $P^{5+}$  is assumed, the effect of Si in the metal on partitioning is very large:  $\varepsilon_P^{Si} = 44.0(\pm 14.7)$  (compared with a best fit value of 13.8 for  $P^{2+}$ ), which is approximately in agreement with Righter et al. (2016), who also determined a large and positive value (of  $\varepsilon_P^{Si} = 66(\pm 15)$ ). However, there is a large scatter in the literature data, where published  $\log(D_P)$  values from different studies are not consistent with one another (Fig. 2). The data of Siebert et al. (2011) and Steenstra et al. (2017b) are most consistent with the results of this study. Such broad scatter between experimental results from different studies may reflect the fact that  $D_P$  is particularly sensitive to silicate melt composition (Hillgren et al., 1996; Righter et al., 2010; Siebert et al., 2011; Steenstra et al., 2017b).

#### 4.4.9 Arsenic

Our values for  $\text{Log}(D_{As})$  are consistent with low-S literature data (Fig. 2; literature data  $P = 0.5 - 18$  GPa). The oxidation state of arsenic in reduced silicate melts is poorly constrained, by both the present data and previous experimental studies. We find the lowest mismatch solution with  $As^{2+}$  and a large interaction with silicon ( $\varepsilon_{As}^{Si} = 24.6$ ). However, the individual data points overlain onto predictive curves (discussed below) do not indicate a coherent result (Fig. S1, supplementary information). Siebert et al. (2011) calculated a mean 5.2+ valence based on the  $D_{As}$  vs.  $fO_2$  slope (range:  $\Delta IW$  approx. -1.5 to -2.5), although there is some scatter in the data. Righter et al. (2017a) found a best fit with  $As^{3+}$ , although their argument is somewhat circular given that they applied an activity correction using  $\varepsilon_{As}^{Si}$  from their own study, which was fitted assuming a 3+ valence state. With no further evidence available, we choose a valence of 3+, based on two coherent  $\log(D_{As})$  data points (Fig. S1, supplementary information) and the suggestion of higher valence from the Si-free metal partitioning experiments of Siebert et al. (2011).  $As^{3+}$  requires a strong interaction with Si ( $\varepsilon_{As}^{Si} = 34.7(\pm 6.8)$ ) to match the data, consistent with the value  $\varepsilon_{As}^{Si} = 35.9$  determined by Righter et al. (2017a) from carbon-free experiments.

$\varepsilon_{\text{As}}^{\text{Si}}$  for other oxidation states, such as 5+, can be obtained using the equation provided in Table 2.

## 5 DISCUSSION

### 5.1 How reliable is the RMS minimisation method for determining valence state?

In this study,  $\varepsilon_{\text{M}}^{\text{Si}}$  and valence are simultaneously determined by finding the combination with the lowest RMS difference between predicted and measured  $\log(D_{\text{M}})$  (valence being an integer). Given how low the RMS uncertainty is for the best fit valence in most cases (Table 2), this appears to be an effective method. However, the results of this method must be interpreted with caution. To understand the meaning of the lowest mismatch result, we can plot predictions of  $\log(D_{\text{M}})$  as a function of  $\Delta\text{IW}$  for different combinations of valence state and  $\varepsilon_{\text{M}}^{\text{Si}}$ , and compare the results with the experimental data (Fig. 5). Each predicted curve is calculated for a particular valence, using the best fit  $\varepsilon_{\text{M}}^{\text{Si}}$  that was fitted for *that specific* valence using the equations provided in Table 2. Higher valence state curves have a steeper curvature at low  $f\text{O}_2$ , as a large calculated Si interaction effect compensates for the steep negative slope predicted from the valence. The intercept is calculated from  $\Delta G^\circ$  at 2600 K and  $X_{\text{Si}}$  is calculated from  $\Delta\text{IW}$  according to the fit of Fig. 3. Zero valence curves are concave-upwards, as without a redox reaction occurring, a slightly negative  $\varepsilon_{\text{M}}^{\text{Si}}$  is required to match the negative slope of the data: given that none of the elements have a zero valence, this situation does not represent reality.

We show three typical examples in Fig. 5; plots for the other elements are shown in the supplementary data (Fig. S1). In all cases, the  $X_{\text{Si}} \sim 0$  data points do not contribute to the determination of the best solution, as they must lie on the intersection of the curves. (1) In the case of Ge (also Cu, Sb, Sn), it is an unfortunate coincidence that the lowest  $f\text{O}_2$ , highest  $X_{\text{Si}}$  point lies near a second intersection, thus contributing little in the discrimination of the best fit curve to the data. The best fit curve is therefore effectively determined by the single data point

at around  $\Delta IW-4$ . This point has a low uncertainty and gives results consistent with the literature, but one should be aware that small changes in this single partition coefficient would change the best fit valence. (2) In the case of Pb (and also Ag, Au), data points have a better spread across an  $fO_2$  range, and so are statistically more useful for constraining the best fit valence state. They lie between the 1+ and 2+ curves, resulting in 1+ and 2+ valence states having almost equally low RMS misfits. In this case, the method is more reliable. (3) In the case of P (and also As), data points fall on different predicted curves that correspond to different valence states. The partition coefficients may not be known precisely enough for this method to work, and there is considerable doubt about the lowest RMS solution (in this case 2+), which evidently represents an average. PO is unlikely to be the stable species because of the electronic configuration of P, so this method is not always effective. It is likely that these highly-charged species are very sensitive to silicate melt composition (e.g. O'Neill et al., 2008), so small variations in the silicate melt could change their activity coefficients and thus their partitioning behaviour. The compositions of silicate melts in this study are all similar, though not identical, and the main variation is in the FeO concentration, which changes as a function of  $fO_2$ .

Ideally, a greater number and spread of experimental data points would make this method more robust. Because this method is not perfect, we chose our preferred valence states by considering Figs. 3 and 5 together with literature data.

## **5.2 Interaction with Si: Implication for apparent valence determinations in partitioning experiments**

In metals, our results show that there is a positive interaction between Si and all moderately volatile elements examined in this study (i.e. all elements become less siderophile to varying extents when Si content of the metal increases). This has implications for the interpretation of partitioning studies. Si is often added to the starting material of multianvil experiments in order to access more reducing conditions (e.g. Gessmann et al., 1999; Mann et al., 2009; Fischer et

al., 2015), and this is especially the case in recent diamond anvil cell partitioning experiments (Siebert et al., 2012, 2013; Fischer et al., 2015). In such cases, Si would reduce the partition coefficient  $D_M$ , perhaps giving the impression of a lower valence state (for example, if a single valence is fitted using a multiple linear regression), or a change to a lower valence state. For example, Gessmann et al. (1999) determined a formal valence for Ni (in ferropericlase at 9 GPa) of  $+1.66 \pm 0.04$ : the deviation from the true oxidation state of +2 indicated that activity corrections in both the metal and oxide phases were required. Capobianco et al. (1999) noted from solid metal-liquid silicate partitioning experiments that the metallic composition (specifically the Ni content, which is added to increase  $fO_2$ ) can affect  $D_{Ga}$ ,  $D_{Ge}$  and  $D_{Sn}$ , and result in the valence being incorrectly assigned; the effect may be stronger in solids, which typically mix less ideally than liquids.

For large volume press experiments that only access the  $fO_2$  conditions which are considered to be realistic for the late stages of core formation ( $\sim \Delta IW -2.0$ ; Frost et al., 2008), little metallic Si should be present, so there should be no significant deviation in  $D$  resulting from Si interaction.

### **5.3 Interaction with Si: Implication for the composition of planetary cores**

Although piston cylinder and multianvil experiments tend to be performed at  $fO_2$  conditions relevant to the segregation of the Earth's core, the lower experimental pressures and temperatures mean that the resulting metals are often low in Si relative to the concentration in the Earth's core. We show that Au, Ag, As, Cu, Sn, Sb, Ge, Cu and P all interact to varying extents with Si, so the lack of metallic Si in such experiments means that partition coefficients for these elements may be overestimated relative to higher pressure core-mantle partitioning behaviour.

It is more important to consider the effect of Si on partitioning at higher  $P$ - $T$  conditions. Diamond anvil cell (DAC) partitioning experiments are usually performed at 30–

100 GPa and  $>3000$  K. The samples resulting from DAC experiments are typically rather oxidised, with high oxygen contents in the metal and high FeO contents in the silicate. Despite this, DAC metals also appear to have high metallic Si contents, i.e. more Si can enter the metal at very high  $P$ - $T$  conditions at a given  $fO_2$  (Takafuji et al., 2005; Bouhifd et al., 2011; Siebert et al., 2012; Fischer et al., 2015). On the basis of their identified  $PT$ -dependencies of  $D_{Si}$  and  $D_O$ , Fischer et al. (2015) calculate that the Earth's core may contain up to 8.5 wt.% Si based on a single-stage core formation model.

A high metallic Si fraction in core-forming metal would decrease  $D$  for all elements, causing higher trace element concentrations in the mantle and lower concentrations in the core. It is therefore important to make activity corrections, for example using the  $\epsilon$  parameters presented here, in order to properly interpret and extrapolate lower-pressure partitioning results to planetary interiors. It is currently not possible to realistically model the moderately volatile element concentrations of the Earth using a heterogeneous accretion and differentiation model, because the  $PT$ -dependencies of some partition coefficients either completely unknown, or the pressure and/or temperature dependences are only known at low pressures (e.g. Ballhaus et al., 2017; Righter et al., 2017a, b; Steenstra et al., 2017a). Additionally, S content will influence partitioning behaviour (Laurenz et al., 2016; Ballhaus et al., 2017), and perhaps also O. To illustrate the magnitude of the effect of metallic Si on core-mantle partitioning of the moderately volatile elements, we instead provide calculations based on single-stage core formation in Fig. 6, based on our experimental conditions of 11 GPa and 2600 K. We stress that single-stage core-mantle equilibration is unrealistic for the complex early history and evolving  $fO_2$  of the growing Earth (e.g. Rubie et al., 2015), and that this calculation is only provided to show a first-order magnitude of the activity effect for 0%, 5% and 10% metallic Si concentrations in the core. The  $fO_2$  was set at  $\Delta IW$ -2.3 and the calculation shows the depletion in the BSE from chondritic based on core formation only, i.e. disregarding any loss due to volatility or incomplete condensation. These simplifications mean that the results are illustrative of the

magnitude of the effect of Si being present, but are not accurate in terms of Earth's differentiation.

The depletion is the concentration remaining in the BSE after core formation ( $C$ ) as a fraction of the initial ( $C_0$ , e.g. chondritic) concentration, and is calculated using:

$$\frac{C}{C_0} = \frac{1}{1 - X_{\text{core}} + D_M X_{\text{core}}} \quad (10)$$

where  $X_{\text{core}}$  is the mass fraction of the core. Fig. 6 shows that all elements become less depleted in the BSE due to core formation with more metallic Si present. Activity terms and oxide valence states are used in the calculation of  $D_M$ . The elements with the largest  $\epsilon$  interaction parameters (As, P and Sb) are the most sensitive to Si content, and 10 mol % Si can decrease their relative depletion by around an order of magnitude. The elements with the smallest  $\epsilon$  are only slightly affected by Si. Even after accounting for metallic silicon, many volatile elements, notably As, Ge and Sb, are still depleted by orders of magnitude relative to the known depletion (if  $C_0$  is taken as the CI chondrite composition of Palme and O'Neill, 2003). This residual difference is presumably due to the effect of volatility, such as partial condensation and/or volatilisation from impacts and magma ocean stages (e.g. Norris and Wood, 2017), in addition to the simplistic nature of the calculation (single-stage core formation, without consideration for the effect of  $P$ ,  $T$ , and other metal and silicate compositional effects on  $D_M$ ).

In reality, some stages during early core formation may have been as reducing as  $\Delta\text{IW}-5$ , resulting in a significant fraction of metallic Si, and later, less reduced stages will be at  $P$ - $T$  conditions that are sufficiently high for Si to continue to enter the core (Rubie et al., 2015). Considering redox equilibria alone (Eq. 2), the lower the  $f\text{O}_2$  of core formation, the higher the partition coefficient  $D_M$  of all cations in the silicate melt is expected to be. However, this effect will be counteracted by the increasing core Si concentration, meaning that partitioning will be less sensitive to  $f\text{O}_2$  than anticipated. This is especially true for the highly charged volatile

cations of this study ( $\text{As}^{3+}$ ,  $\text{Sb}^{3+}$ ,  $\text{P}^{5+}$ ) and also some highly charged refractory cations ( $\text{Mo}^{4+}$  and  $\text{W}^{6+}$ ; Tuff et al. 2011), where a steep slope of  $D_M$  as a function of  $f\text{O}_2$  is expected, yet the increased siderophilicity with decreasing  $f\text{O}_2$  is counteracted by the largest interaction parameters with Si (Table 2 and Tuff et al., 2011). There is a correlation between the size of the  $\epsilon_{\text{Si}}^M$  interaction parameter and the valence state of a cation in the silicate melt, where the neutral forms of highly charged silicate cations interact more strongly with metallic Si in the metal. Since the interaction of Si with the elements studied counteracts the effect of low  $f\text{O}_2$  which normally results in increased siderophile behaviour, reducing conditions in the early stages of core formation do not necessarily result in complete or even strong depletion of siderophile elements when Si is present as a light element in the metal phase. This is an important consideration, given that Si is likely a major contributor to the Earth's core density deficit (Allégre et al., 1995; Gessmann et al., 2001; McDonough, 2003; Ricolleau et al., 2011; Rubie et al., 2011, 2015).

## 6 SUMMARY AND CONCLUSIONS

Based on liquid metal – liquid silicate partitioning experiments addressing a range of volatile siderophile elements (Cu, Ag, Au, Pb, Sn, Ge, Sb, P and As) at 11 GPa and around 2600 K, we show that metal-silicate partition coefficients are always lower than predicted from redox equilibria at  $\Delta\text{IW} < -3$ . We attribute this to the effect of an increased content of Si in the metal: Si increases the activity coefficient of the trace element in question and reduces its siderophilicity. The slope of  $D_M$  as a function of  $f\text{O}_2$  is generally used to determine the valence of the oxide species in the silicate melt. Because Si partitions into the metal at low  $f\text{O}_2$ , the slope of increasing  $\log(D_M)$  with decreasing  $f\text{O}_2$  will become shallower or even reversed, giving a false impression of a decrease in valence state. Therefore, our study joins that of Capobianco et al. (1999) in recommending that appropriate activity corrections are made to experimental partition coefficients before attempting to interpret the valence state of the cation of interest

in silicate melts. At low  $fO_2$ , the correct valence and reaction coefficient can only be determined after appropriate activity corrections for Si have been applied; likewise, corrections need to be applied for Ni interaction in Ni-bearing experiments (Capobianco et al., 1999; Righter and Drake, 2000) and potentially for O or S interaction if they are present in the metal.

For a number of elements examined in this study, the valences of the oxide species in silicate melts have previously been uncertain (e.g. As, Ge, Sn, Au). It is difficult to determine valences for these elements directly from our new data because of the effects of Si on partitioning behaviour. We instead propose a new method to simultaneously solve valence and the Si interaction. Our preferred valences are: Cu, Ag, Au: 1+; Sn, Ge, Pb: 2+; As, Sb: 3+; P: 5+. It was generally found that the elements with the highest valence oxide species also have the highest positive interaction with Si (P and As have the highest  $\epsilon_M^{Si}$ ; Ag and Cu the lowest). This means that their partition coefficients will be the lowest relative to values that are predicted without taking account of the effects of interactions with Si in the metal.

The Earth's core equilibrated at pressures and temperatures much greater than those reached during typical experimental partitioning studies. At such conditions, liquid metal could contain appreciable Si, even under relatively oxidising conditions. This means that the effect of metallic Si on partitioning must be considered when extrapolating experimental partitioning results to core-formation conditions. For each element studied, interaction with Si will counteract the effect of the low  $fO_2$  of core segregation, which normally results in increased siderophile behaviour. These results therefore predict that reducing conditions in the early stages of core formation do not necessarily result in complete or even strong depletion of siderophile elements when Si is present as a light element in core-forming liquid metal.

## 7 ACKNOWLEDGEMENTS

We would like to thank Andreas Audétat for performing the LA-ICP-MS measurements of the silicate glasses, Detlef Krauß for assistance with the microprobe, and Hubert Schulze and

Raphael Njul for sample preparation. We would also like to thank Herbert Palme for helpful discussions throughout this project. We thank three anonymous reviewers for thorough and extensive reviews, which significantly improved the manuscript, and Rajdeep Dasgupta for editorial handling. This work was supported by the German Science Foundation (DFG) Priority Programme SPP1385 “The First 10 Million Years of the Solar System – a Planetary Materials Approach (RU 1323/2) and the European Research Council (ERC) Advanced Grant “ACCRETE” (Contract No. 290568).

## 8 REFERENCES

Albarède F. (2009) Volatile accretion history of the terrestrial planets and dynamic implications. *Nature* **461**, 1227–1233.

Allègre C. J., Poirier J.-P., Humler E. and Hofmann A. W. (1995) The chemical composition of the Earth. *Earth Planet. Sci. Lett.* **134**, 515–526.

Asahara Y., Kubo T. and Kondo T. (2004) Phase relations of a carbonaceous chondrite at lower mantle conditions. *Phys. Earth Planet. Inter.* **143**, 421–432.

Ballhaus C., Fonseca R. O. C., Münker C., Rohrbach A., Nagel T., Speelmanns I. M., Helmy H. M., Zirner A., Vogel A. K. and Heuser A. (2017) The great sulfur depletion of Earth’s mantle is not a signature of mantle–core equilibration. *Contrib. Mineral. Petrol.* **172**, 68.

Ballhaus C., Laurenz V., Münker C., Fonseca R. O. C., Albarède F., Rohrbach A., Lagos M., Schmidt M. W., Jochum K.-P., Stoll B., Weis U. and Helmy H. M. (2013) The U/Pb ratio of the Earth’s mantle—A signature of late volatile addition. *Earth Planet. Sci. Lett.* **362**, 237–245.

- Bennett N. R., Brenan J. M. and Koga K. T. (2014) The solubility of platinum in silicate melt under reducing conditions: Results from experiments without metal inclusions. *Geochim. Cosmochim. Acta* **133**, 422–442.
- Bernstein L. R. (1985) Germanium geochemistry and mineralogy. *Geochim. Cosmochim. Acta* **49**, 2409–2422.
- Borisov A. and Palme H. (1996) Experimental determination of the solubility of Au in silicate melts. *Mineral. Petrol.* **56**, 297–312.
- Bouhifd M. A., Andraut D., Bolfan-Casanova N., Hammouda T. and Devidal J. L. (2013) Metal–silicate partitioning of Pb and U: Effects of metal composition and oxygen fugacity. *Geochim. Cosmochim. Acta* **114**, 13–28.
- Bouhifd M. A. and Jephcoat A. P. (2011) Convergence of Ni and Co metal–silicate partition coefficients in the deep magma-ocean and coupled silicon–oxygen solubility in iron melts at high pressures. *Earth Planet. Sci. Lett.* **307**, 341–348.
- Brenan J. M. and McDonough W. F. (2009) Core formation and metal–silicate fractionation of osmium and iridium from gold. *Nat. Geosci.* **2**, 798–801.
- Capobianco C. J., Dearo J. A., Drake M. J. and Hillgren V. J. (1994) Siderophile Trace Elements in Silicate Melts: Significance and Status of Unusual Oxidation States. 25th Lunar and Planetary Science Conference, Houston.
- Capobianco C. J., Drake M. J. and de'Aro J. (1999) Siderophile geochemistry of Ga, Ge, and Sn: cationic oxidation states in silicate melts and the effect of composition in iron–nickel alloys. *Geochim. Cosmochim. Acta* **63**, 2667–2677.

Chabot N. L., Campbell A. J., Jones J. H., Humayun M. and Lauer Jr. H. V. (2006) The influence of carbon on trace element partitioning behavior. *Geochim. Cosmochim. Acta* **70**, 1322–1335.

Chabot N. L., Safko T. M. and McDonough W. F. (2010) Effect of silicon on trace element partitioning in iron-bearing metallic melts. *Meteorit. Planet. Sci.* **45**, 1243–1257.

Corgne A., Keshav S., Wood B. J., McDonough W. F. and Fei Y. (2008) Metal–silicate partitioning and constraints on core composition and oxygen fugacity during Earth accretion. *Geochim. Cosmochim. Acta* **72**, 574–589.

Danielson L. R., Sharp T. G. and Hervig R. L. (2005) Implications for Core Formation of the Earth from High Pressure-Temperature Au Partitioning Experiments. 36th LPSC. Houston.

Ertel W., Dingwell D. B. and Sylvester P. J. (2008) Siderophile elements in silicate melts — A review of the mechanically assisted equilibration technique and the nanonugget issue. *Chem. Geol.* **248**, 119–139.

Fischer R. A., Nakajima Y., Campbell A. J., Frost D. J., Harries D., Langenhorst F., Miyajima N., Pollok K. and Rubie D. C. (2015) High pressure metal–silicate partitioning of Ni, Co, V, Cr, Si, and O. *Geochim. Cosmochim. Acta* **167**, 177–194.

Frost D. J., Mann U., Asahara Y. and Rubie D. C. (2008) The redox state of the mantle during and just after core formation. *Philos. Trans. R. Soc. Lond. Math. Phys. Eng. Sci.* **366**, 4315–4337.

Frost D. J., Poe B. T., Trønnes R. G., Liebske C., Duba A. and Rubie D. C. (2004) A new large-volume multianvil system. *Phys. Earth Planet. Inter.* **143–144**, 507–514.

Geßmann C. K. and Rubie D. C. (1998) The Effect of Temperature on the Partitioning of Nickel, Cobalt, Manganese, Chromium, and Vanadium at 9 GPa and Constraints on Formation of the Earth's Core. *Geochim. Cosmochim. Acta* **62**, 867–882.

Gessmann C. K., Rubie D. C. and McCammon C. A. (1999) Oxygen fugacity dependence of Ni, Co, Mn, Cr, V, and Si partitioning between liquid metal and magnesiowüstite at 9–18 GPa and 2200°C. *Geochim. Cosmochim. Acta* **63**, 1853–1863.

Gessmann C. K., Wood B. J., Rubie D. C. and Kilburn M. R. (2001) Solubility of silicon in liquid metal at high pressure: implications for the composition of the Earth's core. *Earth Planet. Sci. Lett.* **184**, 367–376.

Hillgren V. J., Drake M. J. and Rubie D. C. (1996) High pressure and high temperature metal-silicate partitioning of siderophile elements: The importance of silicate liquid composition. *Geochim. Cosmochim. Acta* **60**, 2257–2263.

Holzheid A. and Lodders K. (2001) Solubility of copper in silicate melts as function of oxygen and sulfur fugacities, temperature, and silicate composition. *Geochim. Cosmochim. Acta* **65**, 1933–1951.

Holzheid A., Palme H. and Chakraborty S. (1997) The activities of NiO, CoO and FeO in silicate melts. *Chem. Geol.* **139**, 21–38.

Hu M.-Y., Fan X.-T., Stoll B., Kuzmin D., Liu Y., Liu Y., Sun W., Wang G., Zhan X.-C. and Jochum K. P. (2011) Preliminary Characterisation of New Reference Materials for Microanalysis: Chinese Geological Standard Glasses CGSG-1, CGSG-2, CGSG-4 and CGSG-5. *Geostand. Geoanalytical Res.* **35**, 235–251.

Jana D. and Walker D. (1997a) The impact of carbon on element distribution during core formation. *Geochim. Cosmochim. Acta* **61**, 2759–2763.

Jana D. and Walker D. (1997b) The influence of sulfur on partitioning of siderophile elements. *Geochim. Cosmochim. Acta* **61**, 5255–5277.

Jochum K. P., Nohl U., Herwig K., Lammel E., Stoll B. and Hofmann A. W. (2005) GeoReM: A New Geochemical Database for Reference Materials and Isotopic Standards. *Geostand. Geoanalytical Res.* **29**, 333–338.

Jochum K. P., Weis U., Stoll B., Kuzmin D., Yang Q., Raczek I., Jacob D. E., Stracke A., Birbaum K., Frick D. A., Günther D. and Enzweiler J. (2011) Determination of Reference Values for NIST SRM 610-617 Glasses Following ISO Guidelines. *Geostand. Geoanalytical Res.* **35**, 397–429.

JSPS: The Japan Society for the Promotion of Science, The Nineteenth Committee on Steelmaking (1988) *The Steelmaking Sourcebook*. Revised., Gordon & Breach Science Publishers Ltd, New York.

Kegler P. and Holzheid A. (2011) Determination of the formal Ge-oxide species in silicate melts at oxygen fugacities applicable to terrestrial core formation scenarios. *Eur. J. Mineral.* **23**, 369–378.

Lagos M., Ballhaus C., Münker C., Wohlgemuth–Ueberwasser C., Berndt J. and Kuzmin D. V. (2008) The Earth's missing lead may not be in the core. *Nature* **456**, 89–92.

Laurenz V., Fonseca R. O. C., Ballhaus C., Jochum K. P., Heuser A. and Sylvester P. J. (2013) The solubility of palladium and ruthenium in picritic melts: 2. The effect of sulfur. *Geochim. Cosmochim. Acta* **108**, 172–183.

Laurenz V., Rubie D. C., Frost D. J. and Vogel A. K. (2016) The importance of sulfur for the behavior of highly-siderophile elements during Earth's differentiation. *Geochim. Cosmochim. Acta* **194**, 123–138.

Ma Z. (2001) Thermodynamic description for concentrated metallic solutions using interaction parameters. *Metall. Mater. Trans. B* **32**, 87–103.

Malavergne V., Tarrida M., Combes R., Bureau H., Jones J. and Schwandt C. (2007) New high-pressure and high-temperature metal/silicate partitioning of U and Pb: Implications for the cores of the Earth and Mars. *Geochim. Cosmochim. Acta* **71**, 2637–2655.

Mann U., Frost D. J. and Rubie D. C. (2009) Evidence for high-pressure core-mantle differentiation from the metal–silicate partitioning of lithophile and weakly-siderophile elements. *Geochim. Cosmochim. Acta* **73**, 7360–7386.

McDonough W. F. (2003) Compositional Model for the Earth's Core. *Treatise on Geochemistry*. **2**, 568.

Médard E., Schmidt M. W., Wälle M., Keller N. S. and Günther D. (2015) Platinum partitioning between metal and silicate melts: Core formation, late veneer and the nanonuggets issue. *Geochim. Cosmochim. Acta* **162**, 183–201.

Newsom H. E. and Drake M. J. (1983) Experimental investigation of the partitioning of phosphorus between metal and silicate phases: implications for the Earth, Moon and Eucrite Parent Body. *Geochim. Cosmochim. Acta* **47**, 93–100.

Norris C. A. and Wood B. J. (2017) Earth's volatile contents established by melting and vaporization. *Nature* **549**, 507–510.

O'Neill H. S. C. (1991) The origin of the moon and the early history of the earth—A chemical model. Part 2: The earth. *Geochim. Cosmochim. Acta* **55**, 1159–1172.

O'Neill H. S. C., Berry A. J. and Eggins S. M. (2008) The solubility and oxidation state of tungsten in silicate melts: Implications for the comparative chemistry of W and Mo in planetary differentiation processes. *Chem. Geol.* **255**, 346–359.

O'Neill H. S. C., Canil D. and Rubie D. C. (1998) Oxide-metal equilibria to 2500°C and 25 GPa: Implications for core formation and the light component in the Earth's core. *J. Geophys. Res. Solid Earth* **103**, 12239–12260.

Palme H. and O'Neill H. S. C. (2003) Cosmochemical Estimates of Mantle Composition. *Treatise on Geochemistry*, **2**, 1–38.

Ricolleau A., Fei Y., Corgne A., Siebert J. and Badro J. (2011) Oxygen and silicon contents of Earth's core from high pressure metal–silicate partitioning experiments. *Earth Planet. Sci. Lett.* **310**, 409–421.

Righter K. and Drake M. J. (2000) Metal/silicate equilibrium in the early Earth—New constraints from the volatile moderately siderophile elements Ga, Cu, P, and Sn. *Geochim. Cosmochim. Acta* **64**, 3581–3597.

Righter K., Humayun M., Campbell A. J., Danielson L., Hill D. and Drake M. J. (2009) Experimental studies of metal–silicate partitioning of Sb: Implications for the terrestrial and lunar mantles. *Geochim. Cosmochim. Acta* **73**, 1487–1504.

Righter K., King C., Danielson L., Pando K. and Lee C. T. (2011) Experimental determination of the metal/silicate partition coefficient of Germanium: Implications for core and mantle differentiation. *Earth Planet. Sci. Lett.* **304**, 379–388.

Righter K., Nickodem K., Pando K., Danielson L., Boujibar A., Righter M. and Lapen T. J. (2017a) Distribution of Sb, As, Ge, and In between metal and silicate during accretion and core formation in the Earth. *Geochim. Cosmochim. Acta* **198**, 1–16.

Righter K., Pando K., Danielson L. R., Humayun M., Righter M., Lapen T. and Boujibar A. (2016) Effect of Silicon on Activity Coefficients of Siderophile Elements (P, Au, Pd, As, Ge, Sb, and In) in Liquid Fe, with Application to Core Formation. 47th Lunar and Planetary Science Conference. 21-25 Mar. 2016, United States.

Righter K., Pando K. M., Danielson L. and Lee C.-T. (2010) Partitioning of Mo, P and other siderophile elements (Cu, Ga, Sn, Ni, Co, Cr, Mn, V, and W) between metal and silicate melt as a function of temperature and silicate melt composition. *Earth Planet. Sci. Lett.* **291**, 1–9.

Righter K., Pando K., Marin N., Ross D. K., Righter M., Danielson L., Lapen T. J. and Lee C. (2017b) Volatile element signatures in the mantles of Earth, Moon, and Mars: Core formation fingerprints from Bi, Cd, In, and Sn. *Meteorit. Planet. Sci.* **53**, 1–22.

Rubie D. C. (1999) Characterising the sample environment in multianvil high-pressure experiments. *Phase Transit.* **68**, 431–451.

Rubie D. C., Frost D. J., Mann U., Asahara Y., Nimmo F., Tsuno K., Kegler P., Holzheid A. and Palme H. (2011) Heterogeneous accretion, composition and core–mantle differentiation of the Earth. *Earth Planet. Sci. Lett.* **301**, 31–42.

Rubie D. C., Jacobson S. A., Morbidelli A., O’Brien D. P., Young E. D., de Vries J., Nimmo F., Palme H. and Frost D. J. (2015) Accretion and differentiation of the terrestrial planets with implications for the compositions of early-formed Solar System bodies and accretion of water. *Icarus* **248**, 89–108.

Rubie D. C., Ross C. R., Carroll M. R. and Elphick S. C. (1993) Oxygen self-diffusion in Na<sub>2</sub>Si<sub>4</sub>O<sub>9</sub> liquid up to 10 GPa and estimation of high-pressure melt viscosities. *Am. Mineral.* **78**, 574–582.

Schmitt W., Palme H. and Wänke H. (1989) Experimental determination of metal/silicate partition coefficients for P, Co, Ni, Cu, Ga, Ge, Mo, and W and some implications for the early evolution of the Earth. *Geochim. Cosmochim. Acta* **53**, 173–185.

Schönbächler M., Carlson R. W., Horan M. F., Mock T. D. and Hauri E. H. (2010) Heterogeneous Accretion and the Moderately Volatile Element Budget of Earth. *Science* **328**, 884–887.

Siebert J., Badro J., Antonangeli D. and Ryerson F. J. (2012) Metal–silicate partitioning of Ni and Co in a deep magma ocean. *Earth Planet. Sci. Lett.* **321–322**, 189–197.

Siebert J., Badro J., Antonangeli D. and Ryerson F. J. (2013) Terrestrial Accretion Under Oxidizing Conditions. *Science* **339**, 1194–1197.

Siebert J., Corgne A. and Ryerson F. J. (2011) Systematics of metal–silicate partitioning for many siderophile elements applied to Earth’s core formation. *Geochim. Cosmochim. Acta* **75**, 1451–1489.

Steenstra E. S., Lin Y., Dankers D., Rai N., Berndt J., Matveev S. and Westrenen W. (2017) The lunar core can be a major reservoir for volatile elements S, Se, Te and Sb. *Sci. Rep.* **7**, 14552.

Steenstra E. S., Sitabi A. B., Lin Y. H., Rai N., Knibbe J. S., Berndt J., Matveev S. and van Westrenen W. (2017) The effect of melt composition on metal-silicate partitioning of siderophile elements and constraints on core formation in the angrite parent body. *Geochim. Cosmochim. Acta* **212**, 62–83.

Takafuji N., Hirose K., Mitome M. and Bando Y. (2005) Solubilities of O and Si in liquid iron in equilibrium with (Mg,Fe)SiO<sub>3</sub> perovskite and the light elements in the core. *Geophys. Res. Lett.* **32**, L06313.

Thibault Y. and Walter M. J. (1995) The influence of pressure and temperature on the metal-silicate partition coefficients of nickel and cobalt in a model C1 chondrite and implications for metal segregation in a deep magma ocean. *Geochim. Cosmochim. Acta* **59**, 991–1002.

Tsuno K., Frost D. J. and Rubie D. C. (2013) Simultaneous partitioning of silicon and oxygen into the Earth's core during early Earth differentiation. *Geophys. Res. Lett.* **40**, 66–71.

Tuff J., Wood B. J. and Wade J. (2011) The effect of Si on metal-silicate partitioning of siderophile elements and implications for the conditions of core formation. *Geochim. Cosmochim. Acta* **75**, 673–690.

Wade J. and Wood B. J. (2005) Core formation and the oxidation state of the Earth. *Earth Planet. Sci. Lett.* **236**, 78–95.

Wagner C. (1952) *Thermodynamics of alloys*, Addison-Wesley Press.

Walter M. J., Newsom H. E., Ertel W. and Holzheid A. (2000) Siderophile Elements in the Earth and Moon: Metal/Silicate Partitioning and Implications for Core Formation. In *Origin of the Earth and Moon*, University of Arizona Press., Tucson. pp. 265–289.

Wänke H. (1981) Constitution of terrestrial planets. *Phil Trans R Soc Lond A* **303**, 287–302.

Witt-Eickschen G., Palme H., O'Neill H. S. C. and Allen C. M. (2009) The geochemistry of the volatile trace elements As, Cd, Ga, In and Sn in the Earth's mantle: New evidence from in situ analyses of mantle xenoliths. *Geochim. Cosmochim. Acta* **73**, 1755–1778.

Wood B. J. and Halliday A. N. (2010) The lead isotopic age of the Earth can be explained by core formation alone. *Nature* **465**, 767–770.

Wood B. J., Kiseeva E. S. and Mirolo F. J. (2014) Accretion and core formation: The effects of sulfur on metal-silicate partition coefficients. *Geochim. Cosmochim. Acta* **145**, 248–267.

Wood B. J., Nielsen S. G., Rehkämper M. and Halliday A. N. (2008) The effects of core formation on the Pb- and Tl- isotopic composition of the silicate Earth. *Earth Planet. Sci. Lett.* **269**, 326–336.

Wood B. J., Walter M. J. and Wade J. (2006) Accretion of the Earth and segregation of its core. *Nature* **441**, 825–833.

## 9 APPENDIX

### The epsilon activity model of Ma (2001)

The following set of equations are originally from Ma (2001) and were used in this study to calculate activity coefficients in a multi-component liquid alloy, where interactions may be strongly non-ideal. When  $N$  solutes ( $i, j, k..$ ) are present in a predominantly Fe liquid, the activity coefficient of Fe in the metal ( $\gamma_{\text{Fe}}^{\text{met}}$ ) is calculated using:

$$\begin{aligned}
 \ln \gamma_{\text{Fe}}^{\text{met}} = & \sum_{i=2}^N \varepsilon_i^i (x_i + \ln(1 - x)) \\
 & - \sum_{j=2}^{N-1} \sum_{k=j+1}^N \varepsilon_j^k x_j x_k \left( 1 + \frac{\ln(1 - x_j)}{x_j} + \frac{\ln(1 - x_k)}{x_k} \right) \\
 & + \sum_{i=2}^N \sum_{k=2, k \neq i}^N \varepsilon_i^k x_i x_k \left( 1 + \frac{\ln(1 - x_k)}{x_k} - \frac{1}{1 - x_i} \right) \\
 & + \frac{1}{2} \sum_{j=2}^{N-1} \sum_{k=j+1}^N \varepsilon_j^k x_j^2 x_k^2 \left( \frac{1}{1 - x_j} + \frac{1}{1 - x_k} - 1 \right) \\
 & - \sum_{i=2}^N \sum_{k=2, k \neq i}^N \varepsilon_i^k x_i^2 x_k^2 \left( \frac{1}{1 - x_i} \frac{1}{1 - x_k} + \frac{x_i}{2(1 - x_i)^2} - 1 \right)
 \end{aligned} \tag{A1}$$

The activity coefficient of a given solute ( $\gamma_M^{\text{met}}$ ) can then be calculated:

$$\begin{aligned}
\ln \gamma_i^{\text{met}} &= \ln \gamma_{\text{Fe}}^{\text{met}} + \ln \gamma_i^0 - \varepsilon_i^i \ln(1 - x_i) \\
&\quad - \sum_{k=2, k \neq i}^N \varepsilon_i^k x_k \left( 1 + \frac{\ln(1 - x_k)}{x_k} + \frac{1}{1 - x_i} \right) \\
&\quad + \sum_{k=2, k \neq i}^N \varepsilon_i^k x_k^2 x_i \left( \frac{1}{1 - x_i} + \frac{1}{1 - x_k} + \frac{x_i}{2(1 - x_i)^2} - 1 \right)
\end{aligned} \tag{A2}$$

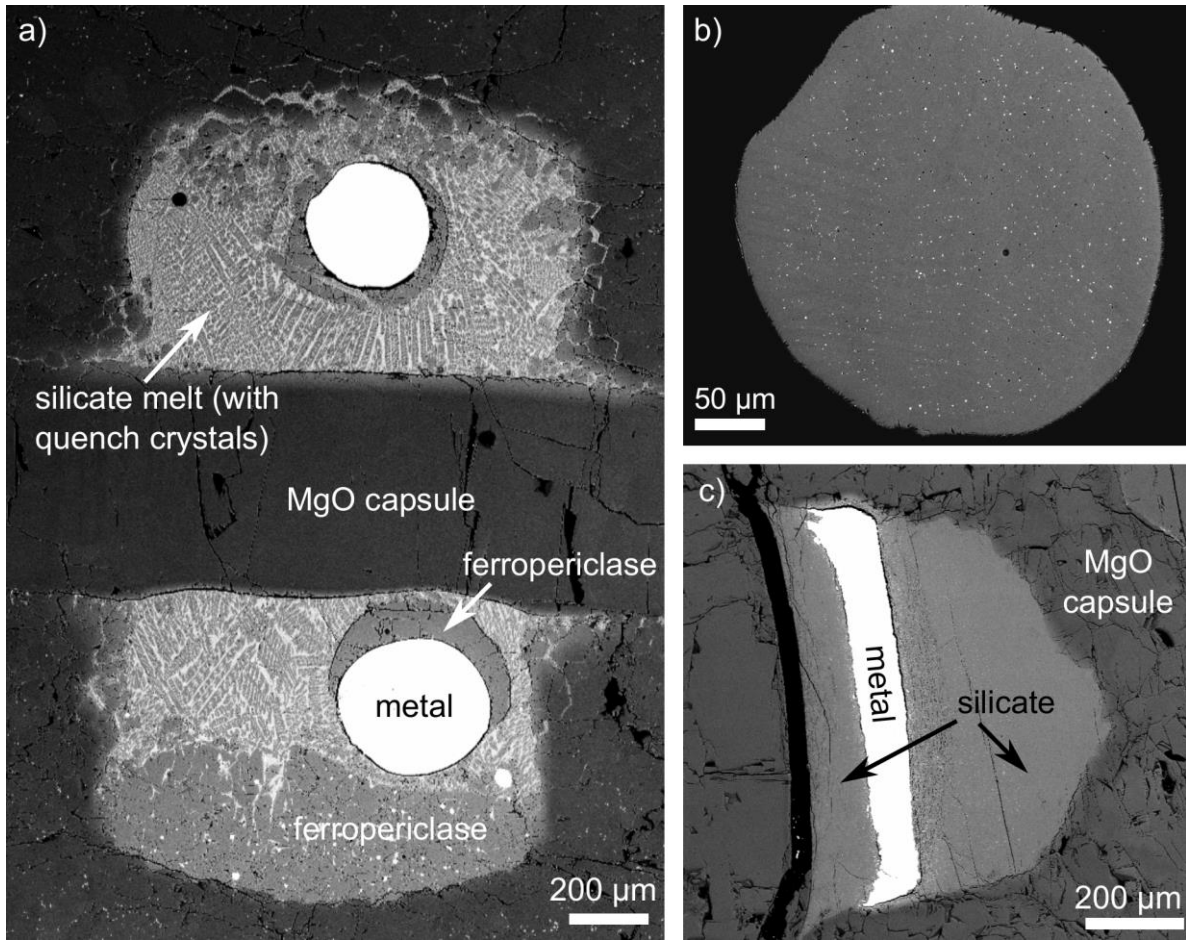
Index  $i=1$  refers to Fe, and  $x_i$  refers to the mole fraction of component  $i$ . To use these equations, epsilon interaction parameters  $\varepsilon_j^k$  (Wagner, 1952) and activity coefficients at infinite dilution ( $\gamma_i^0$ ) of the solute are required. These have a temperature dependence defined in J.S.P.S. (1988) as:

$$\varepsilon_i^j(T_{\text{exp}}) = \frac{T_{\text{ref}}}{T_{\text{exp}}} \varepsilon_i^j(T_{\text{ref}}) \tag{A3}$$

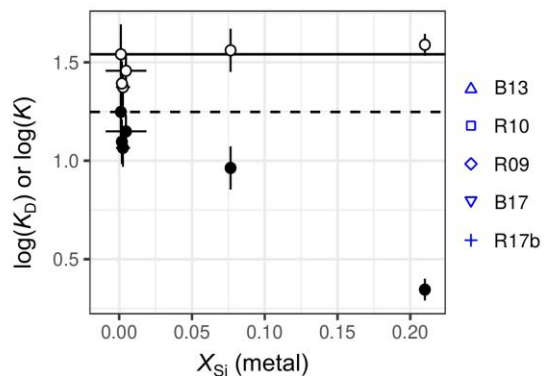
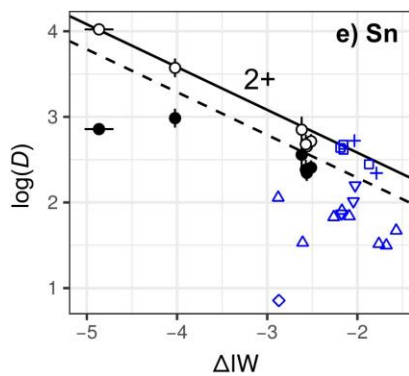
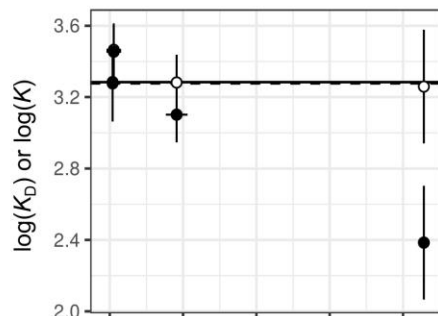
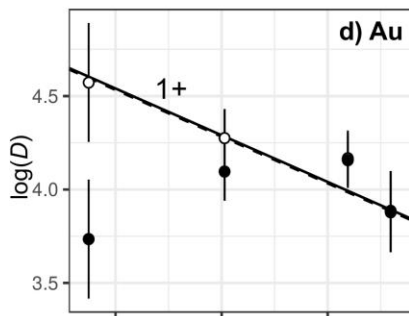
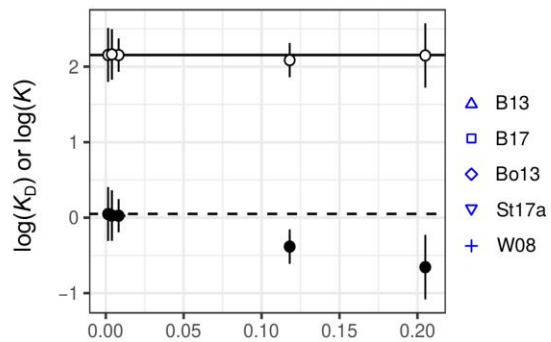
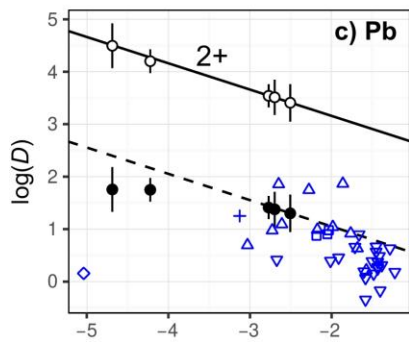
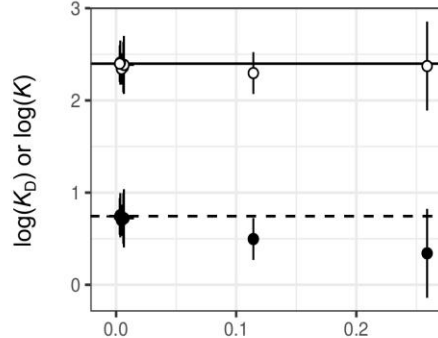
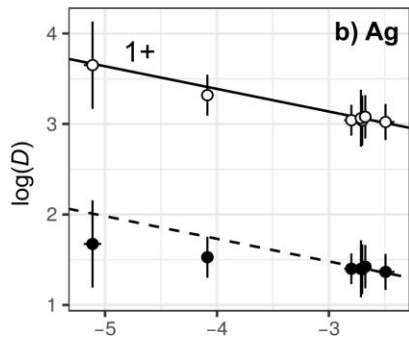
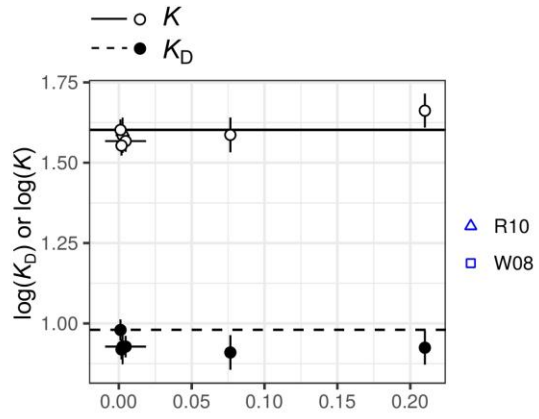
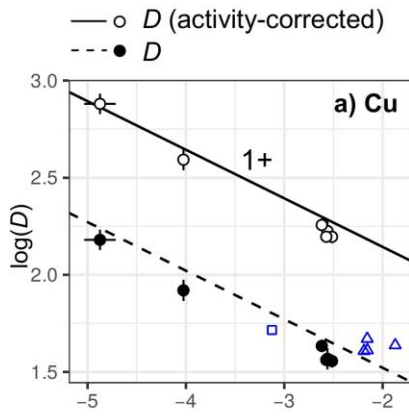
$$\ln(\gamma_M^0(T_{\text{exp}})) = \frac{T_{\text{ref}}}{T_{\text{exp}}} \ln(\gamma_M^0(T_{\text{ref}})) \tag{A4}$$

The required value is that at the experimental temperature,  $T_{\text{exp}}$ .  $\varepsilon_j^k$  and  $\gamma_i^0$  are usually determined and reported at a reference temperature,  $T_{\text{ref}}$ , which is generally 1873 K in J.S.P.S (1988). In this study, our new reported values of  $\varepsilon_M^i$  are also reported at 1873 K for consistency, where they have been converted from the experimental temperature using equation A3.

## 10 FIGURES



**Fig. 1.** Backscattered electron images of a) sample H3444a (top) and H3444b (bottom) that were run simultaneously in a double capsule, showing dendritic olivine quench crystals in the quenched silicate phase; b) the metal phase of sample H3444a showing a typical exsolution texture; c) unsuccessful experiment H3496, which failed to melt. This illustrates the starting setup, where a layer of metal powder was sandwiched between two layers of silicate powder.



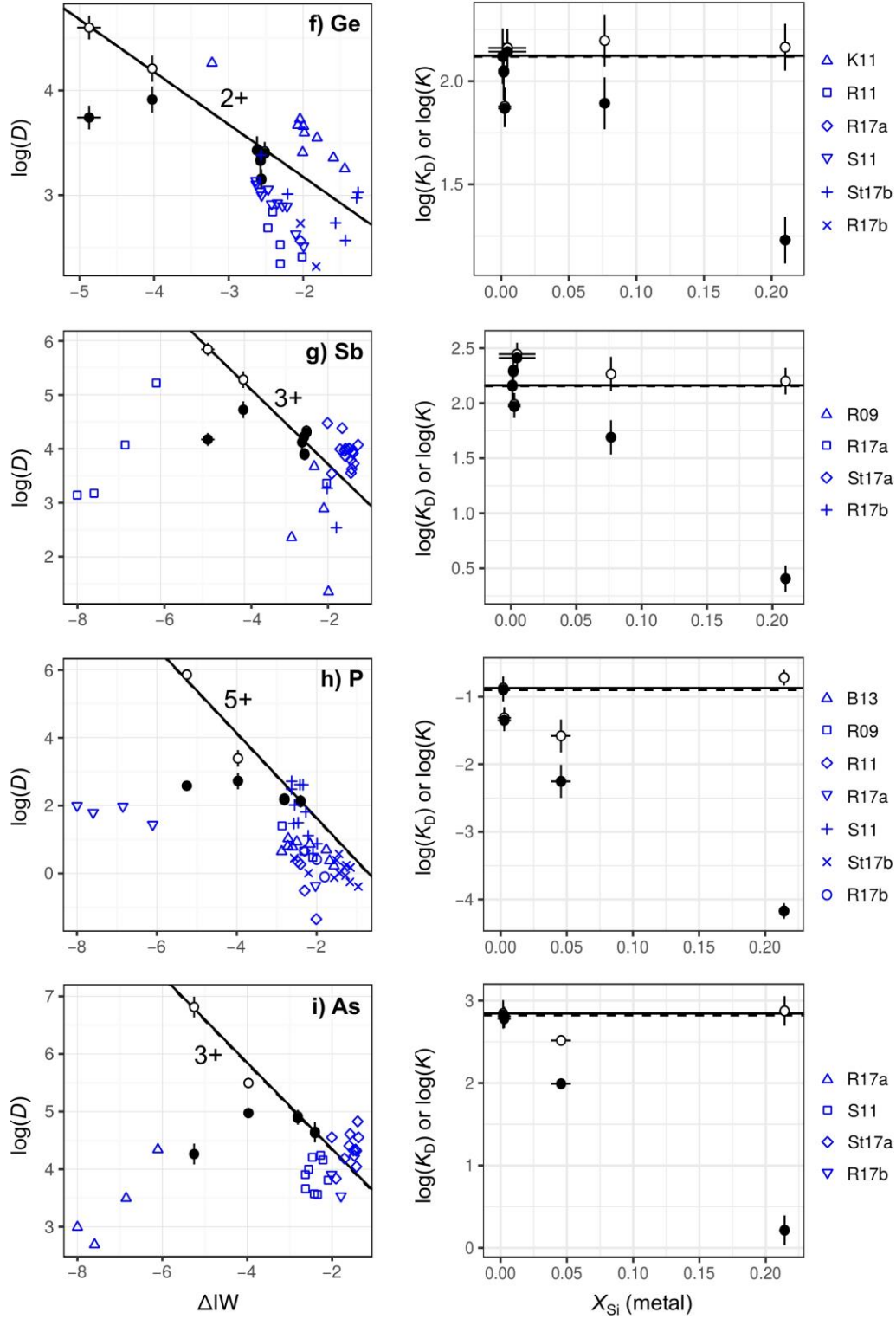


**Fig. 2.**  $\log(D)$  and  $\log(D, \text{activity-corrected})$  as a function of  $\Delta IW$  (left) and  $\log(K_D)$  and  $\log(K)$  as a function of  $X_{Si}$  in the metal (right) of our experiments. Filled symbols represent molar ratios (i.e.  $K_D$  and  $D$ ); open symbols represent activity-corrected molar ratios (i.e.  $K$  and  $D_{\text{activity-corrected}}$ ). Dashed lines are  $\log(K_D)$  and  $\log(D)$  as predicted from the lowest Si experiment and the stated valence; solid lines are  $\log(K)$  and  $\log(D_{\text{activity-corrected}})$  predicted from the lowest Si

experiments (the calculation is explained in section 4.3). Literature  $D$  values are given in blue for comparison: where necessary, these have been converted to mole fraction ratios. References and  $PT$  ranges of published data:

Code	Reference	P (GPa)*	T (K)*
B13	Ballhaus et al. (2013)	1-5	1823-2327
B17	Ballhaus et al. (2017)	1	1773
Bo13	Bouhifd et al. (2013)	8	2373
K11	Kegler and Holzheid (2011)	0.5	1623
R09	Righter et al. (2009)	1.5	1873-1973
R10	Righter et al. (2010)	1	1773-2073
R11	Righter et al. (2011)	1	1773-2173
R17a	Righter et al. (2017a)	1	1873
R17b	Righter et al. (2017b)	1-2	2173
S11	Siebert et al. (2011)	0.5-18	2123-2173
St17a	Steenstra et al. (2017a)	1-2.5	1783-1883
St17b	Steenstra et al. (2017b)	1.5	1783-1883
W08	Wood et al. (2008)	2	2023

\*range of data shown in this figure

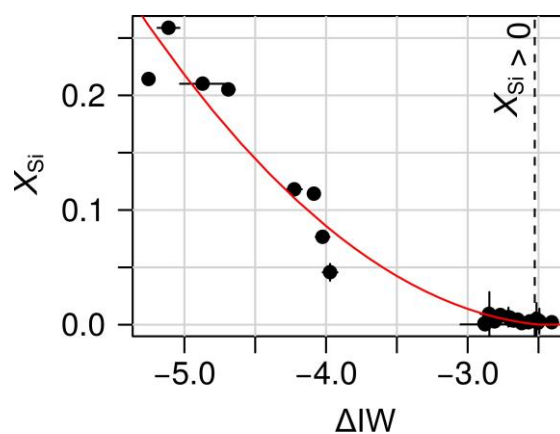


**Fig. 3.**  $X_{Si}$  as a function of  $\Delta IW$  in our experiments, showing that they are negatively correlated. The red curve is a polynomial which has been fitted in order to convert  $\Delta IW$  to  $X_{Si}$  for the calculation of curves in Fig. 5. Above  $\Delta IW$  -2.55,  $X_{Si}$  is assigned to be 0.

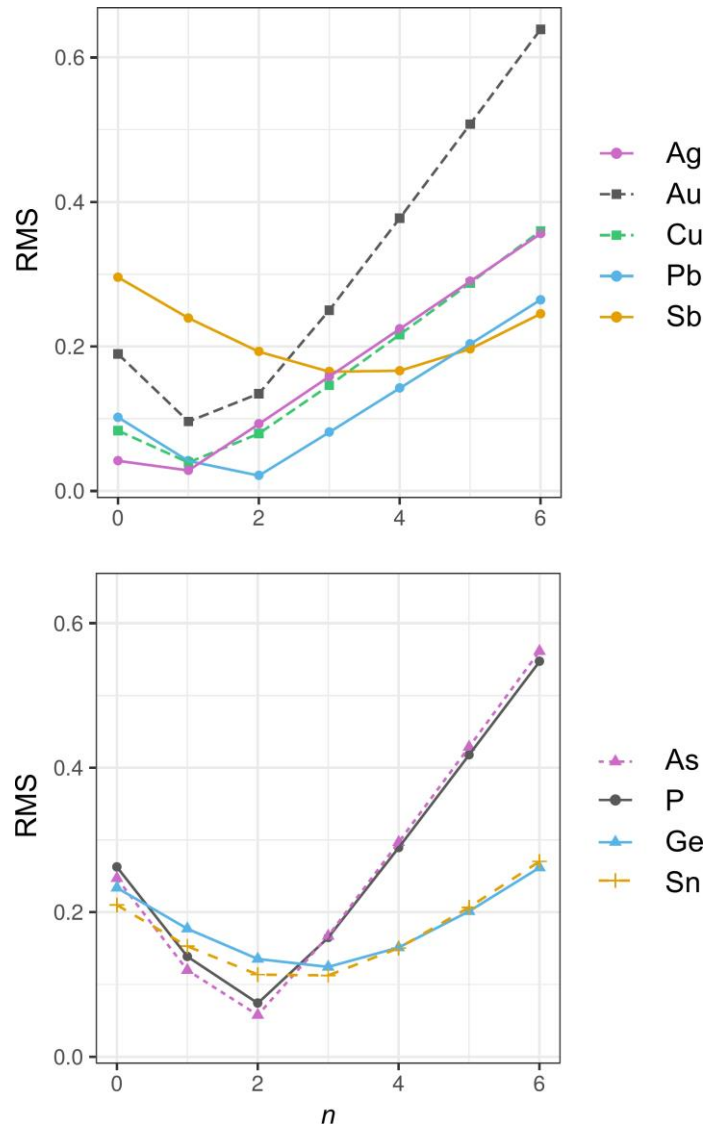


**Fig. 4.** Root mean square (RMS) misfit as a function of valence ( $n$ ) for every element. RMS is a measure of the residual error between predicted and actual  $\log(D_M)$  values after  $\epsilon_M^{Si}$  has been fitted from the data, and the lowest value should indicate the best-fit valence. This figure is presented as two plots for clarity.

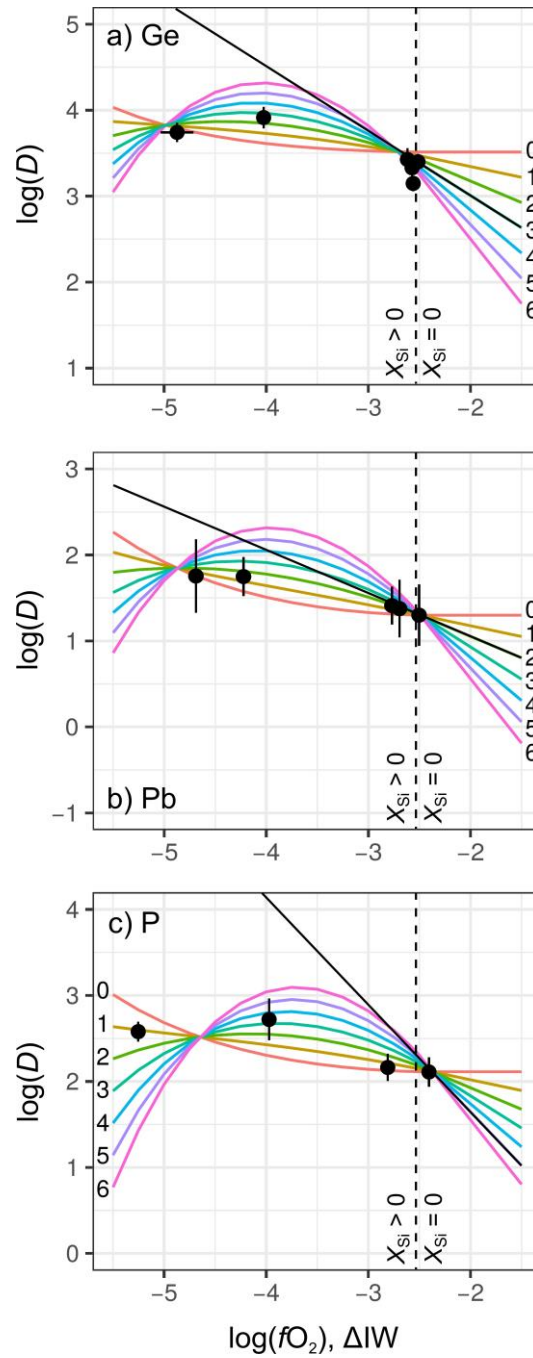


**Fig. 5.**  $\log(D_M)$  as a function of  $\Delta IW$  for a) Ge, b) Pb and c) P in our experiments, overlain onto predicted curves (similar plots for the remaining elements are given in the supplementary information, Fig. S1). Each curve is calculated for a different valence state  $n$ , indicated by the numbers on the left- or right-hand side of the graphs. The curves are predicted from  $X_{Si}$ ,  $n$ , and the best-fit  $\varepsilon_M^{Si}$  for that particular valence state.  $X_{Si}$  is calculated from  $\Delta IW$  according to the polynomial curve of Fig. 3, where  $X_{Si} = 0$  above the  $fO_2$  threshold shown by the vertical dashed line.  $\Delta G^\circ$  for each curve is calculated at 2600 K from the lowest  $X_{Si}$  experiment, meaning that

all curves must intersect (or nearly intersect) at the highest  $\Delta IW$  point by definition. The solid black lines show the predicted trends according to our preferred valence state in the absence of any metallic silicon.

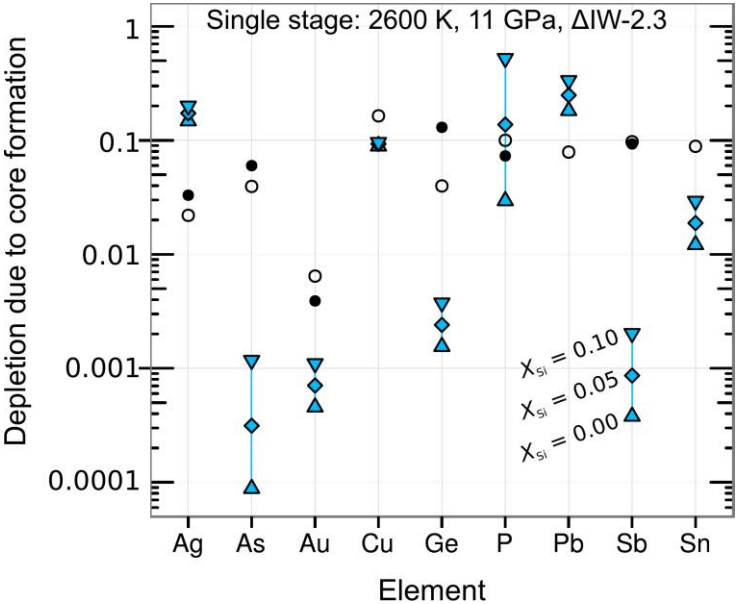


**Fig. 6.** BSE depletion due to core formation of each element of interest, i.e. final silicate concentration as a fraction of the initial. Blue filled symbols are calculated in this study from eq. 10, by considering the effect of the mole fractions of metallic silicon  $X_{Si} = 0$  (triangle), 0.05 (diamond) and 0.1 (inverted triangle) on the partition coefficients. For comparison, open circles are the apparent bulk Earth depletion  $C/C_0$ , where  $C$  is BSE and  $C_0$  is CI chondrite (both compositions Palme and O’Neill, 2003). Filled circles are the apparent bulk Earth depletions including the effect of volatility from Walter et al. (2000).

## 11 TABLES

Experiment	T (K)	$\Delta IW_m^*$	$\sigma$	$\Delta IW_{ac}^*$	$\sigma$	$X_{Si}$	$\sigma$	$\log D_{Cu}$	$\sigma$	$\log D_{Ge}$	$\sigma$	$\log D_{Sb}$	$\sigma$	$\log D_{Sn}$	$\sigma$
H3707a	2584	-2.56	0.04	-2.56	0.04	0.003	0.005	1.57	0.05	3.15	0.09	3.89	0.10	2.35	0.10
H3707b	2584	-5.02	0.16	-4.87	0.16	0.210	0.003	2.18	0.05	3.74	0.11	4.17	0.12	2.86	0.06
H3718a	2658	-2.51	0.03	-2.51	0.03	0.005	0.014	1.56	0.03	3.40	0.09	4.30	0.10	2.41	0.08
H3718b	2658	-4.04	0.05	-4.03	0.05	0.077	0.001	1.92	0.05	3.91	0.13	4.72	0.16	2.98	0.11
Z926a	2668	-2.57	0.03	-2.57	0.03	0.002	0.004	1.56	0.03	3.33	0.13	4.21	0.12	2.38	0.11
Z926b	2668	-2.62	0.03	-2.62	0.03	0.001	0.001	1.63	0.03	3.43	0.13	4.12	0.16	2.56	0.15
								$\log D_{Ag}$	$\sigma$						
H3444a	2609	-2.70	0.03	-2.70	0.03	0.006	0.001	1.40	0.27						
H3444b	2609	-2.80	0.06	-2.80	0.06	0.005	0.001	1.40	0.17						
Z915a	2641	-4.12	0.03	-4.09	0.03	0.114	0.001	1.53	0.23						
Z915b	2641	-5.33	0.08	-5.11	0.08	0.259	0.002	1.67	0.48						
Z916a	2580	-2.71	0.03	-2.71	0.03	0.007	0.008	1.40	0.31						
Z922a	2588	-2.68	0.05	-2.68	0.05	0.003	0.002	1.42	0.24						
Z922b	2588	-2.49	0.08	-2.49	0.08	0.003	0.011	1.37	0.20						
								$\log D_{As}$	$\sigma$	$\log D_{Au}$	$\sigma$	$\log D_P$	$\sigma$		
Z1002b	2602	-3.98	0.05	-3.97	0.05	0.046	0.007	4.98	0.04	4.10	0.16	2.72	0.24		
Z1008b	2614	-2.81	0.06	-2.81	0.06	0.003	0.005	4.89	0.11	4.16	0.15	2.16	0.16		
Z1011a	2605	-2.41	0.05	-2.41	0.05	0.002	0.004	4.63	0.16	3.88	0.21	2.11	0.17		
Z1019b	2624	-5.40	0.04	-5.25	0.04	0.214	0.004	4.26	0.18	3.74	0.32	2.58	0.12		
								$\log D_{Pb}$	$\sigma$						
H3704a	2639	-4.82	0.05	-4.69	0.05	0.205	0.003	1.76	0.43						
H3704b	2639	-4.26	0.05	-4.22	0.05	0.118	0.001	1.75	0.23						
Z919a	2605	-2.77	0.04	-2.77	0.04	0.008	0.004	1.41	0.22						
Z919b	2605	-2.50	0.03	-2.50	0.03	0.001	0.002	1.30	0.36						
Z920b	2580	-2.70	0.05	-2.70	0.05	0.004	0.004	1.38	0.33						

**Table 1:** Results.  $\log(D_M)$  are mole fraction ratios. Complete silicate and metal compositional data are provided as supplementary information.

\*  $\Delta IW_m$  = measured (from  $X_{FeO}/X_{Fe}$ );  $\Delta IW_{ac}$  = activity-corrected. In the text, the activity-corrected version is used unless otherwise specified.

M	$\varepsilon_M^M$	$\ln(\gamma_M^0)$	$\varepsilon_M^{\text{Si}}(n)$	$n$	RMS	$\varepsilon_M^{\text{Si}}$	$\Delta G^0$ (J mol <sup>-1</sup> )
P	7.35	<i>0</i>	$8.1n - 6.5$	5	0.42	44.0 (14.7)	41370
Pb	<i>0</i>	6.73	$8.6n - 7.1$	2	0.02	10.2 (0.9)	-107462
As	<i>0</i>	<i>0</i>	$10.1n + 4.4$	3	0.17	34.7 (6.8)	-142007
Sb	<i>0</i>	<i>0</i>	$7.6n - 0.3$	3	0.17	22.6 (10.6)	-110471
Ge	1.80	<i>0</i>	$7.6n - 3.1$	2	0.14	12.2 (6.3)	-108586
Cu	-5.38	2.15	$7.6n - 6.0$	1	0.04	1.5 (1.1)	-81833
Sn	-0.29	0.95	$7.7n - 3.1$	2	0.11	12.2 (4.9)	-78717
Au	<i>0</i>	<i>0</i>	$10.1n + 1.88$	1	0.10	12.0 (5.2)	-163656
Ag	-18.73	5.30	$7.8n - 2.9$	1	0.03	5.0 (1.3)	-118857

**Table 2:**  $\varepsilon_M^M$ ,  $\varepsilon_M^{\text{Si}}$  and  $\gamma_M^0$  are referenced to 1873 K (equations A3 and A4). Values for  $\varepsilon_M^M$  and  $\gamma_M^0$  are from SDS when available. When unknown, 0 in italics indicates that ideal mixing is assumed.  $n$  is our preferred valence state as discussed in section 4.4, with the subsequent columns calculated on the basis of this value.  $\varepsilon_M^{\text{Si}}(n)$  is  $\varepsilon_M^{\text{Si}}$  as a function of  $n$ , indicating the best fit  $\varepsilon_M^{\text{Si}}$  value that would be obtained if a valence state is assumed that is different from our preferred value.  $1\sigma$  uncertainty on the fitted value of  $\varepsilon_M^{\text{Si}}$  is given in brackets.